Localization and coalescence of imperfect planar FCC truss lattice metamaterials under multiaxial loadings

A.S. Bhuwal[a], T. Liu[b,*], I. Ashcroft[c], W. Sun[a]

[a] *Gas Turbine and Transmissions Research Centre, Faculty of Engineering, University of Nottingham, University Park, Nottingham NG7 2RD, UK*
[b] *Composites Research Group, Faculty of Engineering, University of Nottingham, University Park, Nottingham NG9 5HR, UK*
[c] *Centre for Additive Manufacturing, Faculty of Engineering, University of Nottingham, University Park, Nottingham NG7 2RD, UK*

Abstract

This study investigates the effect of stress triaxiality on the failure mechanisms of anisotropic perfect and imperfect planar FCC (Face Centred Cubic) truss lattice metamaterials. Three types of imperfection have been considered in the numerical modelling, namely, distorted struts, missing struts, and strut diameter variation. In order to maintain constant stress triaxiality during the simulations, a novel numerical framework was developed to overcome computational difficulties within the existing numerical approaches beyond elastic region. Three modes of microscopic localization were observed in perfect and imperfect lattices before failure: crushing band, shear band and void coalescence. A clear separation exists between the three modes of localization depending upon the type and level of defects, as well as the stress triaxiality. Under compressive loading, all lattices fail owing to crushing band; the distorted lattices are prone to shear band localization with increase in distortion, whereas missing lattices majorly fail due to void coalescence at high missing struts defect. Strut diameter variation, within the range of the strut diameters selected, shows no significant influence on the macroscopic mechanical response and strain localization. This work may open the door for predicting failure mechanisms of imperfect lattices under variety of loading conditions.

Keywords: Stress triaxiality, FCC truss lattice metamaterials, Microscopic localization, Shear band, Void coalescence

---

1. Introduction

Additive Manufacturing (AM) technologies have numerous advantages over most traditional manufacturing methods, the most distinct of which is its flexibility to manufacture complex geometries with little or no cost or time penalty [1, 2]. Another advantage

*Corresponding author
Email address: Tao.Liu@nottingham.ac.uk (T. Liu)

is in low volume manufacture, where the lack of moulds or tooling can make AM cost effective, this is especially advantageous for tailored products. AM has spurred recent interest in cellular lattice structures as the technology enables a range of cell types, functional grading and conformity to complex external geometry not achievable with any other manufacturing method [3, 4]. Many researchers are involved in designing complex structures via the use of lattices with different unit cells and relative densities [5]. Köhnen et al. [6] studied plastic deformation behaviour of face centred cubic (f2cc,z) and hollow spherical lattice structures under tensile, compressive and cyclic loadings. In this study f2cc,z lattices revealed a stretch dominated deformation behaviour, while hollowed spherical lattices revealed bending dominated deformation behaviour. Vigliotti et al. [7] established a nonlinear constitutive model for truss lattice materials. In this study, the influence of representative volume element (RVE) is discussed. The hexagonal and the triangulated lattices were selected as case studies and discrete models compared to the prediction of the continuous model. The results found a good qualitative and quantitative agreement among models. Geng et al. [8] showed differences in the fracture modes of three lattice structures and the evolution processes of damage variables using ductile and shear damage models. Alsalla et al. [9] presented a method for estimating the local failure mechanism of 316 L stainless steel lattice material under uniaxial tensile and three-point bending loads. The results show that the tensile strength and fracture toughness of the lattice structure in different directions are different.

The above research demonstrates research in the design of lattices for AM and both experimental and computational analysis of their mechanical properties and failure modes, however, another important aspect that is less studied is the effect of defects on lattice performance. It is inevitable that additively manufactured lattice structures will contain defects not included in the designed (perfect) geometries [10, 11]. Real truss lattices typically contain material and geometric imperfections that may strongly influence their elastic and plastic responses and failure mechanisms. While predictive models of perfect lattices have been used to evaluate both linear and non-linear responses under applied stress [12, 13], they generally fall short in capturing the experimentally observed response of imperfect lattices. Liu et al. [14] investigated the effect of geometric defects on the elastic response, damage initiation and evolution of three-dimensional octet and rhombicuboctahedron periodic structures manufactured by Laser powder bed fusion (L-PBF) process. Wehmeyer et al. [15] presented analytical and reduced-order numerical solutions to predict post buckling behaviour in cellular structures including the role of geometric imperfections. They provided regime maps that shows lattice strut configurations that lead to permanent deformation after unloading, strut failure and enhanced hysteresis during cyclic loading. Other studies on imperfect lattice structures include [16, 17].

In metallic solids, ductile behaviour, and failure mechanisms such as localization and void coalescence are the main failure mechanisms impacting structural integrity. The field

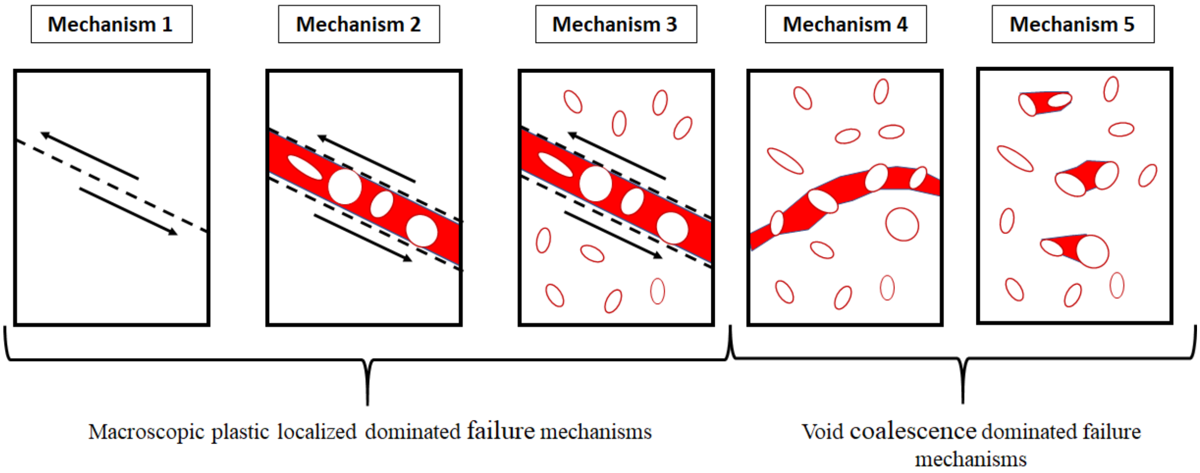

Figure 1: Five generic scenarios of ductile fracture in isotropic solid materials [24]

of ductile fracture has been extensively researched for solid isotropic materials, resulting in more reliable damage models and localization criteria. An example is the recent work related to stress triaxiality dependency [18, 19, 20]. The micro-mechanisms governing ductile shear failure was investigated by Tvergaard et al. [21] using a 2D plane strain numerical cell-model of a single row of equal sized circular cylindrical voids under shearing. As a first, Tvergaard et al. [22] demonstrated that a maximum load bearing capacity for a ductile material was attained in a shear field due to micro-void interaction. Anderson et al. [23] showed that, during shearing, the voids flattened to form micro-cracks, which rotate and elongate until interaction with neighbouring micro-cracks results in coalescence. Failure mechanisms are thereby seen to change with different conditions of stress triaxiality.

The five generic scenarios of localization and void coalescence failure mechanisms in solids are illustrated in Figure 1. Mechanism 1 is localized plastic flow failure in pure metals only, Mechanism 2 is void nucleation after macroscopic localization into shear band, Mechanism 3 is shear band localization owing to porosity present in the metals, Mechanism 4 is failure by void coalescence or occurrence of localization and void coalescence simultaneously, and Mechanism 5 is the subset of Mechanism 4, distinguished as cluster localization of few voids instead of macroscopic localization extending over many voids. The ductile failure of solids is often related to progressive nucleation, growth, and coalescence of micro-voids and microscopic localization.

It is proposed that lattice structures may exhibit comparable mechanisms of micro-localization before final failure depending upon the type of defects and state of stress. It is further proposed that imperfections present in lattices will lead to the onset of microscopic localization or void coalescence, which may serve as an effective indicator of a material's ductility. This is the precursor to failure and marks the limit that a uniform strain can be imposed on the material. Pursuant of this hypothesis, the effects of triaxiality on

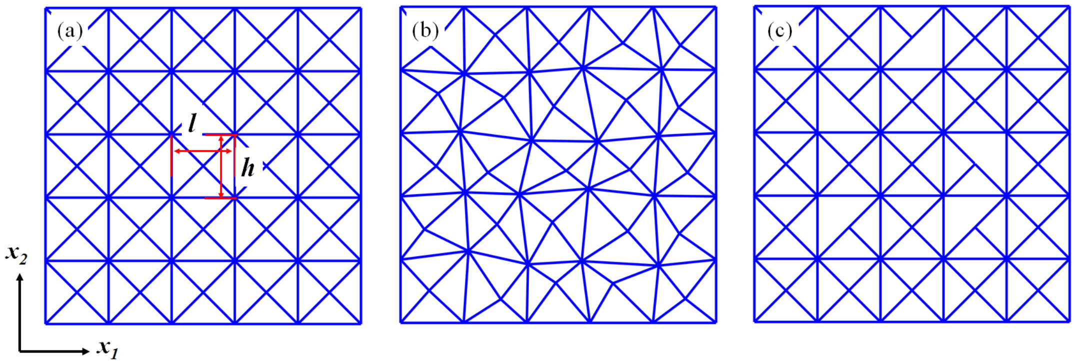

Figure 2: Representation of FCC truss lattice metamaterials with and without manufacturing defects (a) perfect lattice, (b) distorted lattice, and (c) missing struts lattice

imperfect lattices and their failure behaviour are comprehensively studied in this paper for the first time.

The paper is organized as follow. A classification and modelling of lattice defects are presented in Section 2 along with possible failure mechanism identified in this paper. The development of the model, along with numerical implementation is described in Section 3. The results of the numerical simulations are presented and discussed in detail in Section 4. Section 5 contains concluding remarks and suggestions for further research.

2. Imperfect lattice structures and failure mechanisms

2.1. Classification and modelling of imperfect lattices

Common geometric defects in the manufacture of FCC (Face Centred Cubic) truss lattice metamaterials through powder bed fusion can be classified into the following categories [25, 26], as shown in Figures 2 (a) to (c).

1. **Distorted struts** can be characterized by node deviation from the collinear axis of the as-designed struts [27]. As shown in Figure 2 (b), nodal distortion of FCC truss lattices causes misalignment in the attached struts. Modelling of distorted struts was achieved through introducing geometrical perturbation to the nodes of a perfect FCC truss lattice. Let (x_1^i, x_2^i) represent the spatial coordinates of the i^{th} node within a perfect FCC truss lattice. The new position of the node $(\overline{x}_1^i, \overline{x}_2^i)$ after perturbation can be written as:

$$\overline{x}_1^i = x_1^i + \beta\left(\alpha\sqrt{\frac{l^2+h^2}{4}}\right) \tag{1}$$

$$\overline{x}_2^i = x_2^i + \beta\left(\alpha\sqrt{\frac{l^2+h^2}{4}}\right) \tag{2}$$

where $\beta \quad (-1 \leq \beta \leq +1)$ denotes a random variable following a uniform distribution probability distribution, α the degree of irregularity , and l and h are the lengths of the unit cell in the x_1 and x_2 directions, respectively (see Figures 2 (a) and (b)). Romijn and Fleck [28] studied five lattice types, namely Square, Diamond, Hexagonal, Triangular and Kagome, with randomly perturbed nodes in the range of irregularity 0% (perfect lattice) to 50% (extremely imperfect lattice). They showed that the relative density remains the same with perturbed nodes, however, the elastic modulus and fracture toughness are highly sensitive to strut distortion, this also being dependent on the lattice type. In the current paper, degrees of irregularity of $\alpha = 15\%$ and 30% were chosen, in order to prevent impingement of adjacent nodes of FCC truss lattice and to demonstrate strain localization and the effects of a stress state beyond the elastic limit.

2. **Missing struts** are modelled to study the effects of absent struts caused by incomplete fusion in the material. It is generally accepted that randomly missed struts widely exist in lattice structures. The missing struts were modelled in this work through randomly removing struts from a perfect lattice, as illustrated in Figure 2 (c). Let k denote the number of struts that were removed from a lattice of n struts. The level of the manufacturing defect with missing struts can be quantified through $\eta = k/n$. Su et al. [29] and Chen et al. [30] studied missing strut effects ranging from $\eta = 0\%$ to 10% and showed that the mechanical properties of lattice structures are very sensitive to the quantity of missing struts. In the current paper, $\eta = 5\%$ and 10% were selected for the numerical study.

3. **Dimensional inaccuracy** can be caused by over-melting or over heating during LPBF, which results into deviations from circular cross-sections to ellipsoidal [31]. Arabnejad et al. [32] studied such variations in strut diameter and noted a variation from 45% reduction to 100% increase in strut diameter. In this paper, the effect of dimensional inaccuracy on the failure modes of lattices is investigated by the use of three different diameters; $0.5d$, $1.0d$ and $1.5d$ where d is the initial diameter of the struts.

Numerical studies have been carried out to investigate macroscopic elastic behaviour of truss lattices with the defects described above. The studies suggest that the (1) macroscopic elastic and shear moduli are affected by degree of irregularity of distorted lattice albeit only macroscopic shear modulus is affected by missing struts imperfection, and (2) the macroscopic elastic behaviour remains in-plane orthotropic i.e. shear deformation is decoupled from the response in the normal directions; see APPENDIX A.

2.2. Failure mechanisms

In this paper, we have discovered five failure mechanisms of FCC truss lattice metamaterials with and without defects as shown in Figure 3, that are analogous to well-known failure mechanisms seen in isotropic solids. These are discussed below:

1. **Mechanism 1** occurs for lattices buckling predominantly under compressive loading.

2. **Mechanism 2** is analogous to non-porous solid failure due to plastic localization in shear band by various possible mechanisms such as dislocation slipping. Following the formation of the plastic localization inside of band, voids coalesce, leading to final separation. This mechanism occurs due to high stress concentration near a crack tip in solid structures. In lattice structures, lattices with distorted nodes may fail in an analogous fashion due to the abrupt change in load path that this causes.

3. **Mechanism 3** corresponds to the occurrence of localization prior to void nucleation induced by accumulated porosity. Lattices with localized insufficient powder melting and fusion can may have ineffective joining between some struts, which can be considered as having the same effect on mechanical response as a missing strut. The missing struts act as voids in lattice structures and failure occurs owing to shear band formation or strain localization.

4. **Mechanism 4** involves nucleation and localization occurring simultaneously without prior localization owing to the growth mechanism. In this case, the onset of coalescence dictates the onset of macroscopic localization and is caused by missing struts. One of the primary objectives of the present paper is to demonstrate, the different degrees of a particular defect may lead to different failure mechanisms.

5. **Mechanism 5** could be considered as a subcategory of Mechanism 4, i.e. lattices with missing strut defects may have clustering of missing struts which propagates through repeated coalescence. Cluster coalescence will often take place in a region involving a few more closely spaced missing struts and/or experiencing large plastic strain.

3. Numerical framework

Existing numerical studies [20, 33] on the effects of triaxiality for two dimensional or three dimensional solids have been conducted using an implicit finite element (FE) solver such as ABAQUS Standard (Dassault Systemes [34]). The constant triaxiality T was imposed by utilizing a multi-point constraint with the help of user defined subroutines (MPC subroutine in ABAQUS Standard). In the MPC subroutine, user defines constraints to be imposed between different degrees of freedom of ever-changing boundary

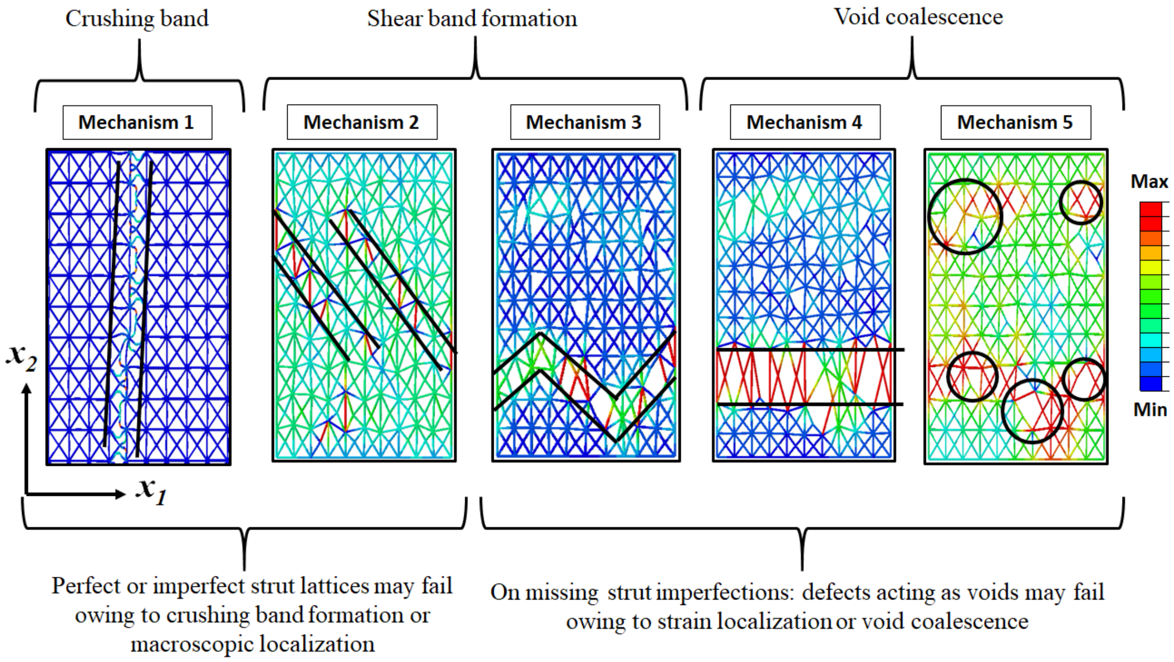

Figure 3: Three failure modes subdivided into five generic scenarios of localization and void coalescence mechanisms observed in lattice structures with and without defects. In Mechanism 1, a perfect lattice is subjected to compressive loading in x_1-direction; In Mechanism 2, an imperfect lattice with 15% distortion is under tension in x_2-direction; In Mechanism 3, a lattice with 5% missing strut is under compression-tension loading with same magnitude in x_1 and x_2 directions, respectively; and In Mechanisms 4 and 5, lattices with 5% missing strut defect are subjected to biaxial tension with different magnitude. The objective of this paper is to distinguish between failure mechanisms associated to different types of defects in FCC truss lattice metamaterials under multiaxial loadings (default ABAQUS color theme has been used to demonstrate logarithmic strain in struts)

conditions, by calculating displacements, iteratively. However, in simulations of complex lattice structures and their post buckling behaviour, the ABAQUS Standard solver may present a convergence issue. To overcome such numerical difficulties, the ABAQUS Explicit solver was employed in the current study. Since the MPC subroutine can not be employed in conjunction ABAQUS Explicit, the following methodology based on constant triaxiality was developed to simulate lattice structures.

Numerical simulations were conducted to investigate FCC truss lattice metamaterials under plane stress as the out-of–plane thickness of a truss lattice is much smaller than the in-plane dimensions and the loads are applied in-plane. Consider the representative volume element (RVE) of a FCC truss lattice under the global coordinate system $x_1 - x_2 - x_3$ subjected to in-plane principle stretches λ_1 and λ_2, as shown in Figure 4 (a), as well as principle out-of-plane stretch λ_3. The RVE consists of k_1 unit cells and has a bulk volume of Ω ($\Omega = W_1 \times W_2 \times d$) at the deformed configuration. A shear band localization containing failed struts may form within the lattice under the stretches. Let ξ_i (i = 1, 2, 3) denote the local coordinate systems that are attached to the band with ξ_1 perpendicular to the shear band, ξ_2 aligned with the longitudinal direction, and ξ_3 aligned with x_3. We

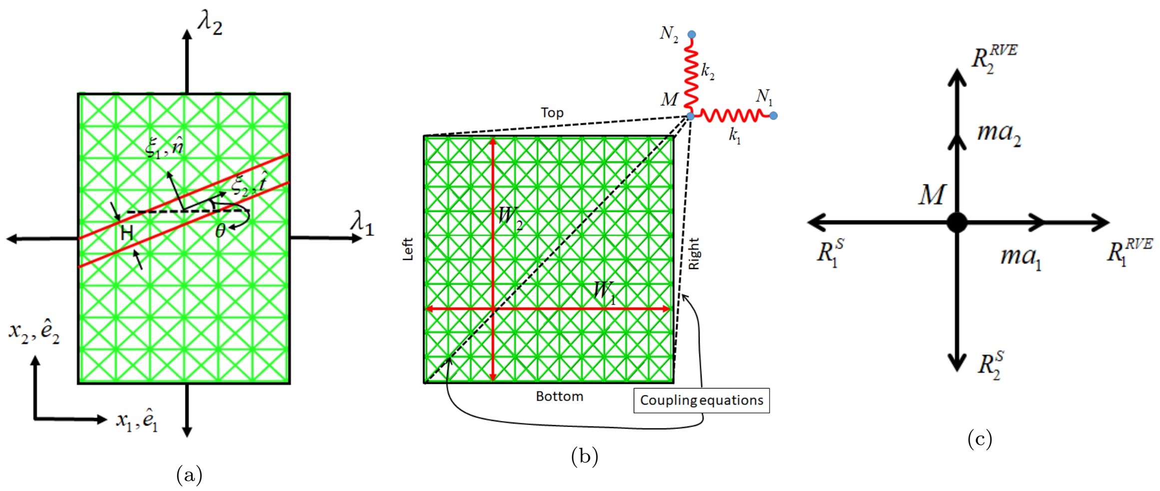

Figure 4: (a) 2-dimensional structure with predefined band subjected to multi-directional stretch, (b) the top, bottom, left and right surfaces of RVE subjected to constraints imposed by a dummy node M, so that the concentrated forces applied to node M by the springs are fully transmitted to the RVE, and (c) the free body diagram of the dummy node M, showing the forces acting on node from RVE ($R_j^{RVE}, j = 1, 2$), spring (R_j^S) and dynamic inertia (ma_j)

introduce vectors $\hat{\mathbf{e}}_i$ aligned with global coordinates x_i; $\hat{\mathbf{n}}$ and $\hat{\mathbf{t}}$ aligned with band local coordinates ξ_1 and ξ_2, respectively. The applied strain components in the remote area parallel to principal axes lead to stress state with principal stress components $(\Sigma_{11}, \Sigma_{22})$, i.e.

$$\mathbf{\Sigma}^0 = \Sigma_{11}\hat{\mathbf{e}}_1 \otimes \hat{\mathbf{e}}_1 + \Sigma_{22}\hat{\mathbf{e}}_2 \otimes \hat{\mathbf{e}}_2 \tag{3}$$

The stress triaxiality T and effective stress Σ_{eff}, describing the stress state, can be defined as

$$T = \frac{\Sigma_{11} + \Sigma_{22}}{3\Sigma_{eff}} \tag{4}$$

or

$$T = \frac{\text{sign}\,(\Sigma_{22})\,(1+\rho)}{3\sqrt{(\rho^2 + 1 - \rho)}} \tag{5}$$

where $\Sigma_{eff} = \sqrt{\frac{1}{2}\left[(\Sigma_{11} - \Sigma_{22})^2 + (\Sigma_{11})^2 + (\Sigma_{22})^2\right]}$ and $\rho = \Sigma_{11}/\Sigma_{22}$.

The numerical simulations were performed under constant T or constant ρ using the method described below. A dummy node, M, which is not part of the structure, was created to impose boundary conditions, see Figure 4 (b). Let u_1^M and u_2^M denote the displacements of M; (u_{left_1}, u_{left_2}), $(u_{right\_1}, u_{right\_2})$, (u_{top_1}, u_{top_2}), and $(u_{bottom\_1}, u_{bottom\_2})$ the displacement nodes on the left, right, top and bottom edges of the RVE, respectively. The displacements of the nodes on the top, bottom, left, and right edges were coupled to the corresponding displacements of node M by means of periodic boundary conditions

(PBCs) [35] defined by the following equations

$$u_{right\_1} - u_{left\_1} = u_1^M \quad \text{and} \quad u_{top\_2} - u_{bottom\_2} = u_2^M \tag{6}$$

In this way, the point force applied to node M is fully transmitted to the lattice structure. The macroscopic stresses acting on the lattice structure can be expressed as:

$$\Sigma_{11} = \frac{R_1^{RVE}}{A_1}, A_1 = \left(\overline{W}_2 + u_2^M\right) d \quad \text{and} \quad \Sigma_{22} = \frac{R_2^{RVE}}{A_2}, A_2 = \left(\overline{W}_1 + u_1^M\right) d \tag{7}$$

where R_j^{RVE} $(j = 1, 2)$ denotes the concentrated force corresponding to the x_j direction of node M; A_1 and A_2 are the areas of the left/right and top/bottom edges of the RVE, respectively; d the strut diameter; $\overline{W}_1$ and $\overline{W}_2$ widths of the RVE in the initial configuration in x_j direction. Two additional dummy nodes N_j are created and connected to dummy node M using a spring element of spring stiffness coefficient $\overline{k}_j$ (SpringA element of the ABAQUS element library [34]) as shown in Figure 4 (b). Hence, the force R_j^S transmitted from nodes N_j to node M can be calculated as:

$$R_j^S = \overline{k}_j \left(u_j^M - u_j^{N_j}\right) \tag{8}$$

where $u_j^{N_j}$ is the displacement of node N_j. Hence, the point forces acting on the RVE, R_j^{RVE}, can be calculated by applying force equilibrium (Figure 4 (c)).

$$R_j^{RVE} = \overline{k}_j \left(u_j^{N_j} - u_j^M\right) - m a_j \tag{9}$$

where m and a_j are the mass and acceleration in x_j direction at node M, respectively. Hence, to keep the stress triaxiality constant, the following parameters need to be satisfied at each incremental strain,

$$\rho = \frac{\Sigma_{11}}{\Sigma_{22}} = \text{ const } \Rightarrow \frac{\left\{\overline{k}_1 \left(u_1^{N_1} - u_1^M\right) - m a_1\right\} \left(\overline{W}_1 + u_1^M\right) d}{\left\{\overline{k}_2 \left(u_2^{N_2} - u_2^M\right) - m a_2\right\} \left(\overline{W}_2 + u_2^M\right) d} = \rho \tag{10}$$

If the mass m and accelerations a_j at node M are nullified by using very small mass (10^{-8}), Equation (10) becomes

$$\begin{aligned} &\rho = \frac{\Sigma_{11}}{\Sigma_{22}} = \text{ const } \Rightarrow \rho = \overline{\overline{k}}\overline{u} \\ &\text{with} \\ &\overline{\overline{k}} = \begin{Bmatrix} \overline{k}_1 \\ \overline{k}_2 \end{Bmatrix}, \quad \overline{u} = \begin{Bmatrix} \dfrac{\left(u_1^{N_1} - u_1^M\right)\left(\overline{W}_1 + u_1^M\right)}{\left(u_2^{N_2} - u_2^M\right)\left(\overline{W}_2 + u_2^M\right)} \end{Bmatrix} \end{aligned} \tag{11}$$

In the above equation, the displacement components $u_1^{N_1}$ and $u_2^{N_2}$ are prescribed values for node N_j. The displacement components of node M at each increment can be calculated through Equation (6). Note that, in Equation (11), we can tune the values of $\overline{\overline{k}}$ and $\overline{u}$ to maintain ρ constant using the method described below.

Numerical calculations suggested u_1^M and u_2^M were very small quantities, i.e. $u_j^M \ll \overline{W}_j$. Hence, we controlled $\overline{u} \approx -1$ or 1 (depending upon the state of stresses) via prescribing very large values to $u_1^{N_1}$ and $u_1^{N_2}$ ($u_1^{N_1}$=$u_2^{N_2}$). Therefore, a constant triaxiality could be maintained by maintaining a constant $\overline{\overline{k}}$. In the numerical simulations, the kinetic energy of the system was maintained at less than 5% of its internal energy to ensure that the process was quasi-static. The ABAQUS Standard solver is not subject to convergence issue for all cases. Hence, the current methodology using ABAQUS Explicit solver was compared with ABAQUS Standard solver results for possible cases without any convergence issues. The results are presented in APPENDIX B, which shows that the two methodologies are comparable.

Under the principle stretches, the macroscopic logarithmic strain tensor $\mathbf{E}^0$ and rate of deformation $\dot{\mathbf{E}}^0$ read

$$\mathbf{E}^0 = E_{11}\hat{\mathbf{e}}_1 \otimes \hat{\mathbf{e}}_l + E_{22}\hat{\mathbf{e}}_2 \otimes \hat{\mathbf{e}}_2 + E_{33}\hat{\mathbf{e}}_3 \otimes \hat{\mathbf{e}}_3 \tag{12}$$

$$\dot{\mathbf{E}}^0 = \dot{E}_{11}\hat{\mathbf{e}}_1 \otimes \hat{\mathbf{e}}_1 + \dot{E}_{22}\hat{\mathbf{e}}_2 \otimes \hat{\mathbf{e}}_2 + \dot{E}_{33}\hat{\mathbf{e}}_3 \otimes \hat{\mathbf{e}}_3 \tag{13}$$

where the components of the two tensors can be calculated as:

$$E_{ii} = \frac{1}{\Omega}\int_\Omega \varepsilon_{ii} d\Omega = \ln \lambda_i, \quad \dot{E}_{ii} = \frac{1}{\Omega}\int_\Omega \dot{\varepsilon}_{ii} d\Omega = \frac{1}{\lambda_i}\dot{\lambda}_i \tag{14}$$

where ε_{ii} ($i = 1, 2, 3$) denotes the microscopic logarithmic strain within the RVE. Next, we consider strain inside the shear band. At the current configuration, the averaged logarithmic strain inside the band of thickness H at an angle θ , with respect to coordinate x_1 (Figure 4 (a)), is equal to the sum of uniform strain in remote area plus the additional strain associated with additional band displacements Δ_1 and Δ_2 under the local coordinates ξ_i ($\hat{\Delta} = \Delta_1\hat{t} + \Delta_2\hat{n}$). The averaged logarithmic strain rate tensor within the band $\dot{\mathbf{E}}^b$ can be written as:

$$\dot{\mathbf{E}}^b = \dot{\mathbf{E}}^0 + \left(1 - \frac{\Omega_b}{\Omega}\right)\left(\frac{\dot{\Delta}_1}{H}\hat{\mathbf{t}} + \frac{\dot{\Delta}_2}{H}\hat{\mathbf{n}}\right) \otimes \hat{\mathbf{n}} = f\left(\dot{\lambda}_1, \dot{\lambda}_2, \dot{\Delta}_1, \dot{\Delta}_2, \theta\right) \tag{15}$$

The following method was employed to calculate $\dot{\mathbf{E}}^b$ in the simulations. Let Ω^b denote the volume of a shear band at the deformed configuration, see Figure 4 (a). The averaged logarithmic strain rate tensor in the band can be described as:

$$\dot{\mathbf{E}}^b = \dot{E}^b_{ij}\hat{\mathbf{e}}_i \otimes \hat{\mathbf{e}}_j \tag{16}$$

with the components of the tensor calculated as:

$$\dot{E}^b_{ij} = \frac{1}{\Omega^b} \int_{\Omega^b} \dot{\varepsilon}^b_{ij} d\Omega \tag{17}$$

where $\dot{\varepsilon}^b_{ij}$ denotes the microscopic logarithmic strain rate within the band. The formation of localization in lattice structures is difficult to visualize due to the presence of randomly distributed defects in a large domain. To calculate ε^b_{ij} and visualize band strain, the nodal displacements at joints of FCC truss lattices were extracted from the detailed FE solutions and used as the input to create a continuum plot of the displacement field using 2D triangular solid elements. The microscopic strain tensor inside the band can be calculated using the finite element formulation described in APPENDIX C.

The accumulated equivalent logarithmic strain within the band and far field can be defined by Hill's equivalent strain [36] (APPENDIX A), given as

$$E_{eq} = \sqrt{\frac{1}{FH + FG + GH} \left[(F + H) (E_{11})^2 + 2H (E_{11} E_{22}) + (G + H) (E_{22})^2 \right] + \frac{2 (E_{12})^2}{I}} \tag{18}$$

where F, G, H, and I are material constants which characterize the degree of anisotropy. The ratio between the equivalent strain within the band E^b_{eq} and macroscopic equivalent strain E_{eq} plays an important role in the identification of failure mechanisms, i.e.

$$E^b_{eq}/E_{eq} = \phi \left(\dot{\lambda}_1, \dot{\lambda}_2, \dot{\Delta}_1, \dot{\Delta}_2, \theta \right) \tag{19}$$

The additional band displacements Δ_1, Δ_2 and shear band angle θ would vanish if no localization takes place in lattice structure.

3.1. Failure mechanisms criterion

Macroscopic localization occurs when parts of a lattice in a band plastically deform while remote regions remain elastic. This criterion is used to identify localization of the structure, i.e. (1) when E^b_{eq}/E_{eq} increases exponentially, the onset of localization occurs; and (2) when E^b_{eq}/E_{eq} exceeds the threshold value of 10 the onset of coalescence occurs [18]. Figure 5 is a schematic plot of the evolution of strain inside a localization band with respect to the remote strain. Mechanisms 1, 2, and 3 are crushing/shear band formation and failure is by crushing/shear band formation, where E^b_{eq}/E_{eq} increases exponentially. In case of failure dictated by onset of coalescence the value of E^b_{eq}/E_{eq} starts at a higher than the threshold value and failure occurs owing to Mechanism 4. In Mechanism 5 the value of E^b_{eq}/E_{eq} increase monotonically above the threshold as E_{eq} increases.

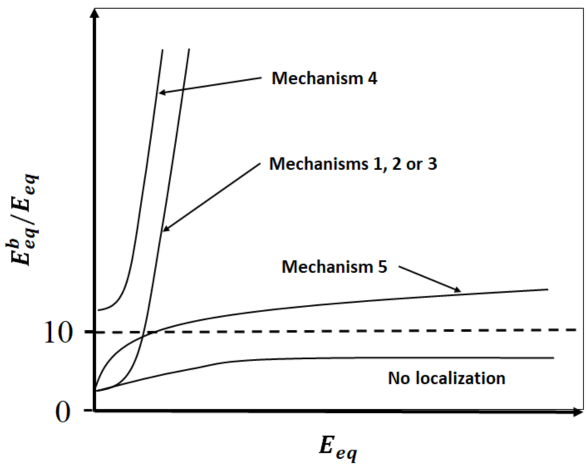

Figure 5: Schematic diagram of evolution of normalized equivalent band strain against equivalent remote strain

3.2. Finite element model

The struts of the FCC truss lattice metamaterials (Figure 2) have been modelled as 2 -node Timoshenko-beam element (B21 in ABAQUS notation) with rigid connections between struts. In the numerical simulations, each strut is modelled as a uniform circular cross sectioned solid bar of diameter d, with equal length and height ($l = h$) for perfect lattice. The relative density $\overline{\rho}$ of the FCC unit cell truss lattice material (ratio of the density of the lattice material to the density of the solid material from which it is made) is given by

$$\overline{\rho} = (1 + \sqrt{2}) \left(\frac{\pi}{2}\right) \left(\frac{d}{l}\right) \tag{20}$$

The strength of a stretch dominated lattice structure with 10% relative density is three times stronger than to an equivalent bending dominated foams [37, 38]. Thus, the value of the relative density was taken as 0.10 ($d = 0.528$ mm, $l = 20$ mm) for our investigation, taking manufacturability of the minimum strut diameter into consideration [39]. Numerical tests have suggested that converged results can be achieved with each strut meshed with 5 beam elements of equal length. Failure events, such as first localization and void coalescence, have been observed to occur at small strains (< 0.01), and the struts have not been found to be in contact during deformation. Hence, contact among struts owing to large deformation has not been modelled. Further numerical studies have suggested that distorted struts have negligible effect on the relative density and for lattices with missing struts, a constant relative density has been achieved by a slight increase in the diameter of the struts.

3.3. Material model

The Ramberg-Osgood model, Equation (21), was used to represent the true stress-strain relationship of the material in the numerical study, as illustrated in Figure 6 [40].

$$\varepsilon = \frac{\sigma}{E} + \alpha \left(\frac{\sigma}{\sigma_y} \right)^n \tag{21}$$

where $E = 71300$ MPa and $\sigma_y = 168$ MPa are parent material's Young's modulus and yield stress respectively; $\alpha = 0.002$ is the yield offset and $n = 9.9$ is the hardening exponent. This material model is suitable to capture the mechanical behaviour of aerospace-grade lightweight aluminum alloys such as AlSi10Mg alloy.

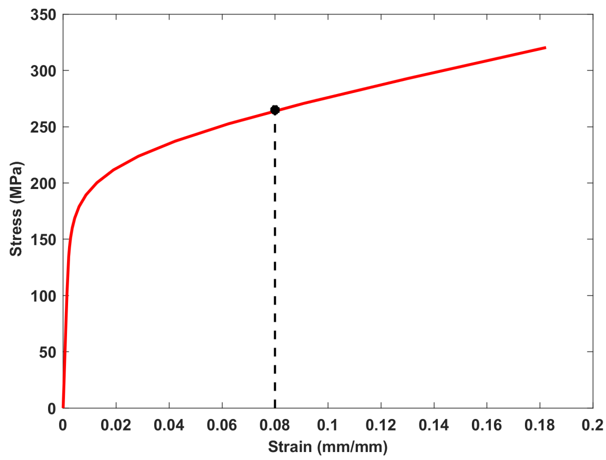

Figure 6: Stress strain curve of the parent material with failure strain ($\varepsilon_f = 0.08$) used for the FE analysis

To study failure mechanisms, the local tensile strain (LTS) criterion was employed in the numerical study. Materials such as high strength aluminum alloys fail due to shear localization when the maximum tensile strain is reached, hence the LTS criterion is appropriate for this study. Rosenthal et al. [40] showed elongation at failure varied between 8-9% for AlSi10Mg specimens manufactured using LPBF. Hence, it is assumed that when the maximum tensile strain in a lattice reaches a failure strain of $\varepsilon_f = 0.08$, failure occurs, and the simulation is terminated. It is noted that material damage has not been considered in the above-mentioned constitutive model.

3.4. Representative volume element (RVE)

An RVE should contain sufficient unit cells to be representative of the bulk mechanical behaviour and lattice failure mechanisms but be minimized to prevent excessive computational cost. Cohen et al. [41] stated that equilibrium solutions in the non-linear regime are not unique, and therefore the response of a truss lattice can depend significantly on the RVE size. To predict the non-linear behaviour of a truss lattice structure, several

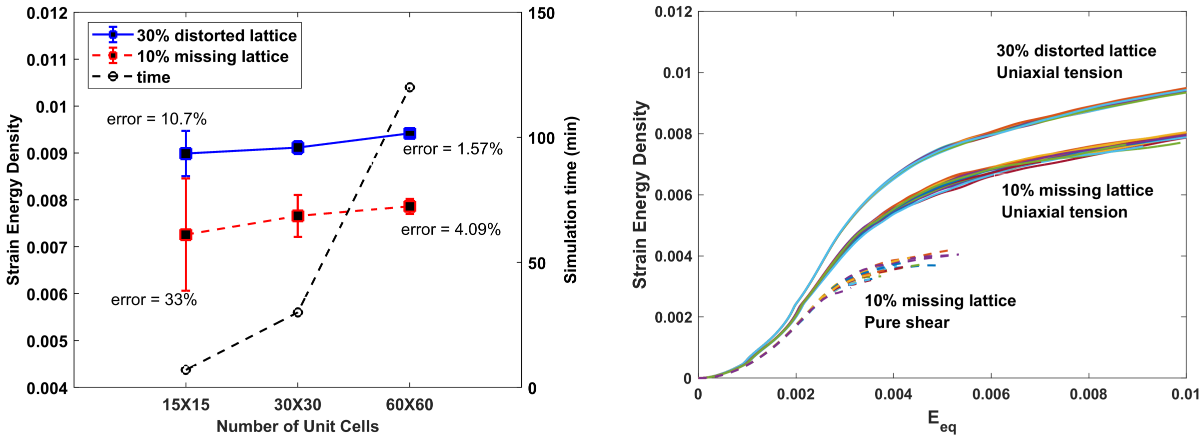

(a) (b)

Figure 7: (a) Strain energy density convergence plot verses number of unit cells in RVE with 30% distorted and 10% missing lattices at $E_{eq} = 0.01$ and simulation time verses unit cells under uniaxial tension, and (b) strain energy density as a function of equivalent strain for RVE containing 60×60 unit cells, with 30% distorted struts and 10% missing struts, under uniaxial tension and pure shear.

RVEs comprising increasing number of unit cells must be numerically tested until convergence is obtained. Therefore, numerical simulations were conducted to evaluate the effect of the size of RVE. The increase in computational time with respect to increase in number of unit cells is shown in 7 (a). The strain energy densities under uniaxial tension with equivalent strain $E_{eq} = 0.01$ were calculated for the RVEs containing 15×15, 30×30 and 60×60 unit cells with two types of defect; 30% distorted and 10% missing struts, as shown in Figure 7 (a). During the simulations, all the lattices and their respective imperfections were generated using the algorithm described in Section 2 with 20 repetitions. The results suggest that (*i*) the strain energy density for the RVE containing 60×60 unit cells can converge to within 5% deviation; (*ii*) the variation of strain energy density for distorted imperfection is much less than that of missing struts imperfection for RVEs containing 15×15 and 30×30 unit cells. Figure 7 (b) shows the strain energy density as a function of equivalent strain for the RVE containing 60×60 unit cells with 30% distorted struts and 10% missing struts, under uniaxial tension and pure shear. Again, the results confirm the convergence of strain energy density for the RVE containing 60×60 unit cells. Henceforth, all the numerical simulations have been carried out using the RVE containing 60×60 unit cells.

4. Results and discussion

4.1. Effect of imperfections on failure locus

Figure 8 (a) shows the failure loci of FCC truss lattice metamaterials under multiaxial loadings obtained by FE simulations. Four quadrants of the failure loci have been plotted for the perfect, 15% distorted and 5% missing struts lattices, respectively. The lattices were subjected to (1) biaxial tension in the first quadrant, (2) biaxial compression in the third quadrant and (3) combination of tension and compression loadings in the second and fourth quadrants. The failure loci are approximately symmetrical about the line where triaxiality $T = -0.67$ and $T = 0.67$. It is evident that lattice imperfection significantly reduces the failure stress within the first quadrant; whereas the effect of imperfection is less pronounced in the other quadrants. In the first quadrant $\Sigma_{11} \geq 0, \Sigma_{22} \geq 0$, the failure stress of the perfect lattice is significantly higher than the imperfect lattices as there is not any arbitrary change in load path and, hence, no localization occurs. In the second quadrant, $\Sigma_{11} \leq 0, \Sigma_{22} \geq 0$, the failure mechanisms of crushing band and shear band (Mechanisms 1, 2, 3, and 4) dictate failure for all types of lattices, resulting in an insignificant impact on the failure strength between the different lattices. In the third quadrant, $\Sigma_{11} \leq 0, \Sigma_{22} \leq 0$ and triaxiality $T < -0.2$, the perfect and imperfect lattices all fail owing to the formation of a crushing band (Mechanism 1) under compression; this shows that, both the stress triaxiality and initial imperfections have significant effects on the failure mechanisms in other quadrants. Figure 8 (b) shows two distinct functional relations between triaxiality T and stress ratio ρ, i.e., $\Sigma_{22} > 0$ and $\Sigma_{22} < 0$. In the following sections, our discussion will focus on the failure mechanisms in the first and second quadrants owing to the symmetric nature of the failure loci: this corresponds to the scenarios with $T \in [-0.2, 0.67]$ and $\Sigma_{22} > 0$.

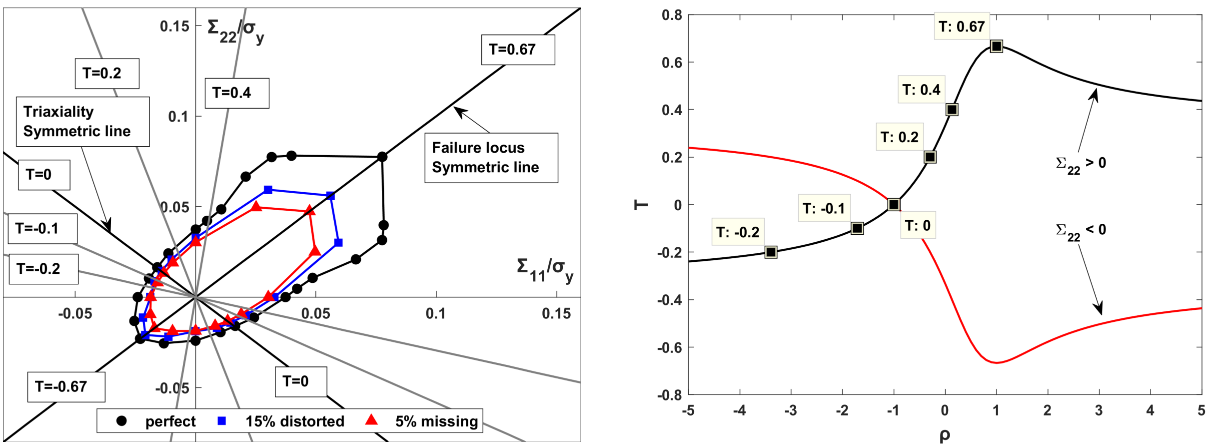

(a) (b)

Figure 8: (a) Failure locus of perfect and imperfect lattice structures and (b) stress triaxiality verses stress ratio taken for numerical simulations.

4.2. *An illustrative example - pure shear loading* ($T = 0$)

In this section the mechanical response and failure mechanisms are discussed for various different lattice cases; a perfect lattice and imperfect lattices with distorted strut defects (15% and 30%) and missing struts (5% and 10%), subjected to a constant triaxiality ($\Sigma_{11} = -\Sigma_{22}, T = 0$, pure shear loading). Results will be presented for the effect of stress triaxiality in later sections.

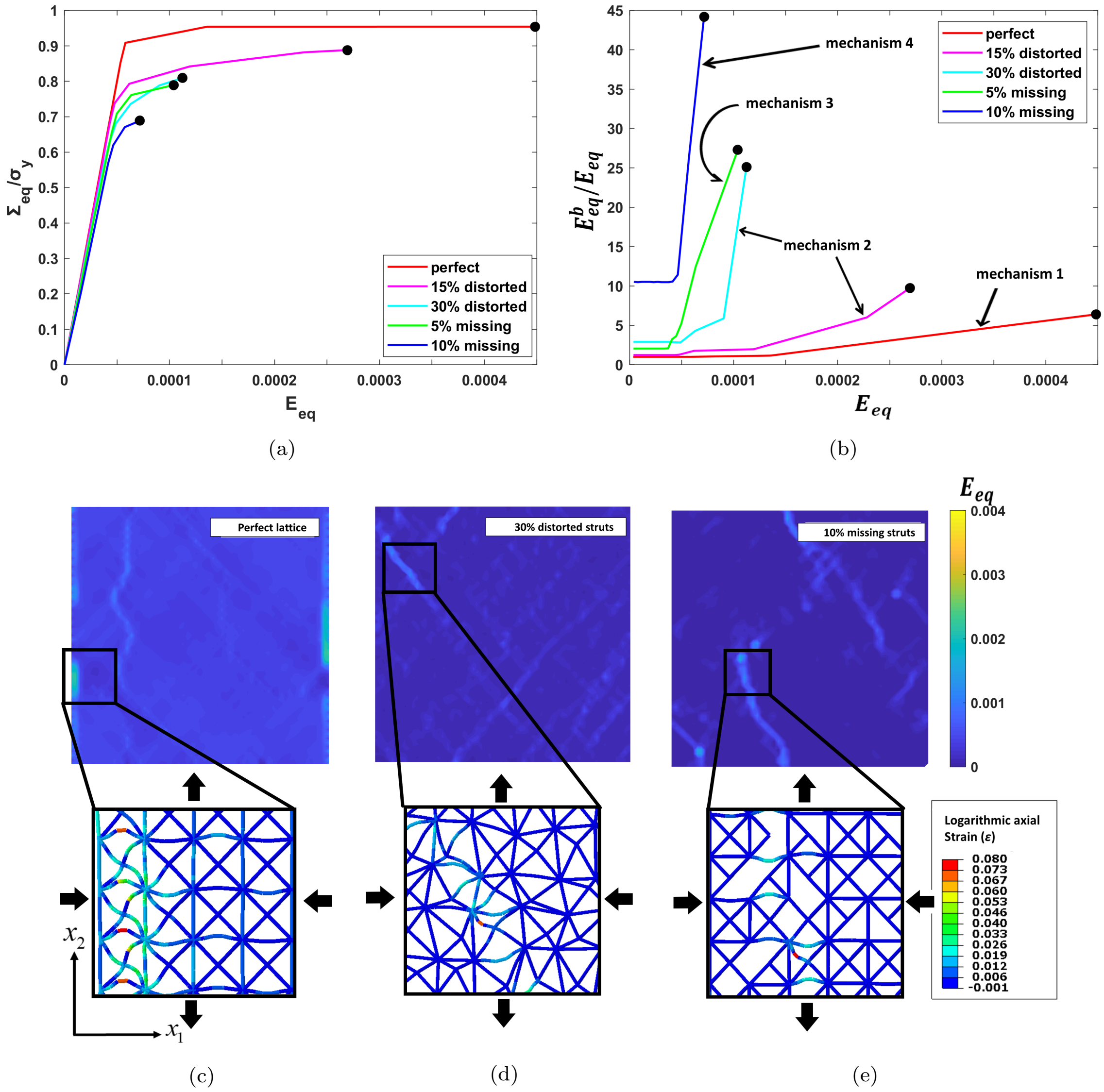

Figure 9: Failure mechanisms comparison of lattices under pure shear (a) variation of normalized macroscopic stress against equivalent remote strain of perfect and imperfect lattices; (b) evolution of normalized equivalent band strain against equivalent remote strain of perfect and imperfect lattices; (c), (d) and (e) equivalent strain continuum plots of RVE, when the maximum strain reached ($\varepsilon_f = 0.08$) for prefect, 30% distorted and 10% missing strut lattices, respectively.

Figure 9 (a) shows the normalized effective stress as a function of remote equivalent strain, E_{eq}, for perfect and imperfect lattices. The perfect lattice has the highest load carrying capacity and ductility. The missing strut defects cause the lattice to fail at much lower effective strains and lower stresses than the corresponding lattices with distorted strut defects. Figure 9 (b) shows the normalized equivalent band strain, E^b_{eq}/E_{eq}, as a function of the remote equivalent strain, E_{eq}, for the perfect lattice and imperfect lattices with selected imperfections. The failure points of the lattices are marked as 'filled circle' on the curves. The failure mechanisms of the perfect lattice, imperfect lattices with the 30% distorted strut defects and the 10% missing strut defects are shown in Figures 9 (c) to (e), respectively. Equivalent strain continuum plots are shown, as well as detailed views of the failed areas. To calculate equivalent strain, the nodal displacements at the joints of the FCC truss lattices were extracted from the FE solutions and used as inputs to calculate strain at each integration point, using 2D triangular solid elements (APPENDIX C). There is no shear localization in the perfect lattice and failure occurs due to crushing band formation (Mechanism 1) under compressive stress ($\Sigma_{11} = -\Sigma_{22}$) with the maximum normalized equivalent band strain less than 5. Strain localization occurred in the lattices with the 15% and 30% distorted strut and missing strut imperfections, respectively. For the 10% missing struts lattices, the normalized equivalent band strain is around 10 at the onset of shear band formation (Figure 9 (b)), which suggests that void coalescence dictates the start of macroscopic localization (Mechanism 4). For the imperfect lattices with 15%, 30% distorted struts and 5% missing struts, the normalized equivalent band strains are less than 5 before the onset of shear band formation (Figure 9 (b)), which suggests that the strain localization is not dictated by the onset of coalescence.

4.3. The effect of stress triaxiality on failure localization

The effect of triaxiality on failure mechanisms is investigated in this section through comparison of the behaviour of (1) a perfect lattice and imperfect lattices with 15% distortion (Figure 10 (a)) and 5% missing struts (Figure 10 (b)); (2) imperfect lattices with 15% and 30% distortion (Figure 10 (c)); and (3) imperfect lattices with 5% and 10% missing struts (Figure 10 (d)). In these figures, the normalized equivalent band strain, E^b_{eq}/E_{eq}, is plotted as a function of the remote effective strain, E_{eq}. To facilitate interpretation of the results, Figures 11 and 12 show the continuum plots and details of the failed areas for the imperfect lattices with 15% distortion and 5% missing strut imperfections, respectively, at selected triaxialities.

Perfect lattice - For triaxialities $T \leq 0$, the perfect lattice has a high normalized equivalent band strain which shows failure due to crushing band formation under compression. For triaxialities $T > 0$, the perfect lattice tends to fail at very high macroscopic strain and does not show any strain localization dominated failures.

15% distorted lattice - For the 15% distorted strut lattice, the maximum normalized equivalent band strain is higher or close to 10 at triaxialities $T < 0$, which signifies the occurrence of strain localization. As shown in Figure 11 (a) at triaxiality $T = -0.2$, the lattice fails owing to crushing band formation (Mechanism 1). A band of localized high strain can be seen in both the continuum plot and detailed beam element figure. It can also be observed that from Figures 11 (b) and (c) (triaxialities $T = -0.1$ and 0), the structure fails due to shear band localization (Mechanism 2). From triaxialities $T > 0$, strain localization does not occur, and multiple high equivalent strain areas can be observed (Figures 11 (d), (e) and (f)).

5% missing struts - For all triaxialities, the 5% missing strut lattices (Figure 10 (b)) show failure occur due to strain localization. The normalized equivalent band strain is less than 5 before onset of the shear band formation, which suggests that the strain localization is not dictated by the onset of coalescence (i.e. Mechanism 3). At triaxiality $T = -0.2$ (Figure 12 (a)), compressive loading pre-dominates, and lattice struts fail owing to crushing band formation (Mechanism 1). At triaxialities $T = -0.1$, 0 and 0.1 (Figures 12 (b) to (d)), shear strain localization (Mechanism 3) becomes noticeable. At triaxiality $T = 0.4$, the normalized equivalent band strain does not increase exponentially and strain localization is dictated by the cluster localization (Figure 12 (e), Mechanism 5) and at triaxiality $T = 0.67$, the normalized equivalent band strain is below the threshold value hence no localization occurs (Figure 12 (f)).

30% distorted lattice - For triaxiality $T < 0$, the failure mechanisms for the 30% distorted lattice are similar to those of the 15% distorted lattices (Figure 10 (c)) i.e. Mechanisms 1 and 2. For triaxiality $0 \leq T \leq 0.4$, the maximum normalized equivalent band strain for the 30% distorted lattice is much higher than that for the 15% distorted lattice, which indicates strain localization dominated failure. At triaxiality $T = 0.67$, strain localization does not occur, and multiple high equivalent strain areas form, as with the 15% distorted lattice.

10% missing struts - The 10% missing struts lattice fails on the formation of a crushing band at triaxiality $T = -0.2$. For triaxialities $T = -0.1$, 0 and 0.2, the normalized equivalent band strains are higher than 10 before onset of the strain localization (Figure 10 (d)), which suggest that void coalescence dictates the onset of strain localization (Mechanism 4). For triaxialities $T = 0.4$ and 0.67, the normalized equivalent band strains do not increase exponentially, and the maximum normalized equivalent band strains are more than 10, which suggests that the strain localization is dictated by the cluster localization (Mechanism 5).

It can be seen from the above that lattice imperfections affect the onset of localization effects, leading to lattice failure. Failure, therefore, involves a number with transition points between mechanisms, which are discussed further in APPENDIX D.

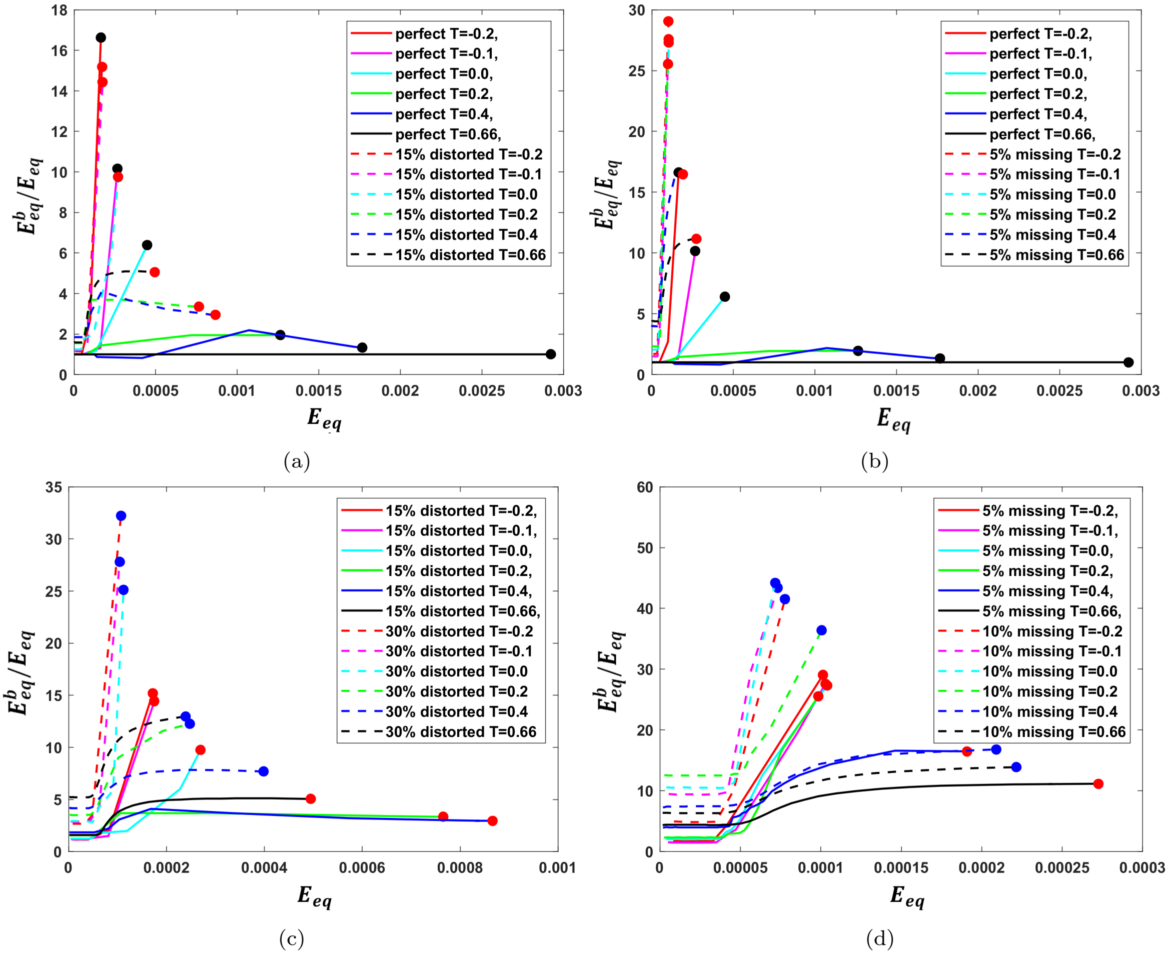

Figure 10: Evolution of equivalent band strain with varying triaxiality from −0.2 to 0.67. Comparison for (a) perfect vs 15% distorted struts, (b) perfect vs 5% missing struts, (c) distorted struts 15% vs 30% and (d) missing struts 5% vs 10%

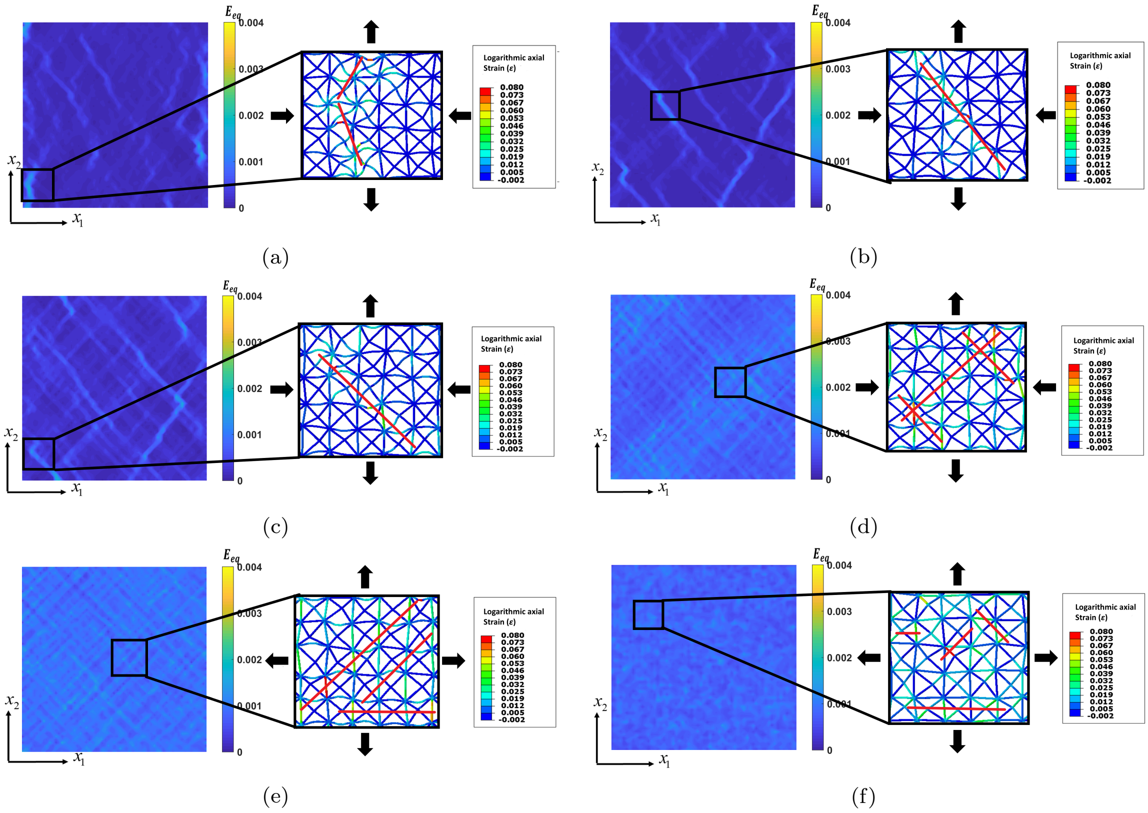

Figure 11: 15% distorted lattices at the point of failure illustrating failure mechanisms on continuum and lattice level at triaxiality (a) $T = -0.2$, (b) $T = -0.1$, (c) $T = 0.0$, (d) $T = 0.2$, (e) $T = 0.4$ and (f) $T = 0.67$

4.4. Effects of size parameter on mechanical response and onset of localization

To explore the significance of dimensional inaccuracy of FCC truss imperfect lattices on mechanical response and localization, we have studied two variants of diameter of struts $0.5d$ and $1.5d$. For brevity, the responses of the imperfect lattices with the 15% distorted struts and 5% missing struts subjected to different triaxiality at constant relative density are shown in Figure 13. In Figures 13 (a) and (c), the normalized effective stress response, Σ_{eq}/σ_y, is plotted against effective remote strain, E_{eq}, for the 15% distorted and 5% missing lattices, respectively. The response graph shows that, irrespective of the size of struts, the maximum load bearing capacity of the imperfect lattices does not show significant difference at equal relative densities. Figure 13 (b) shows the strain localization with varying triaxiality for the 15% distorted lattice. The normalized equivalent band strain curves for both strut diameters follow the same path and fail at nearly the same points. At triaxiality $T = -0.2$, $0.5d$ lattice fails owing to Mechanism 1 and $1.5d$ fails owing to Mechanism 2. For rest of the triaxialities ($T > -0.2$), the failure mechanisms are again not sensitive to the size of the struts. Again, the failure mechanisms of 5% missing lattice are not much affected by the strut diameter (Figure 13 (d)).

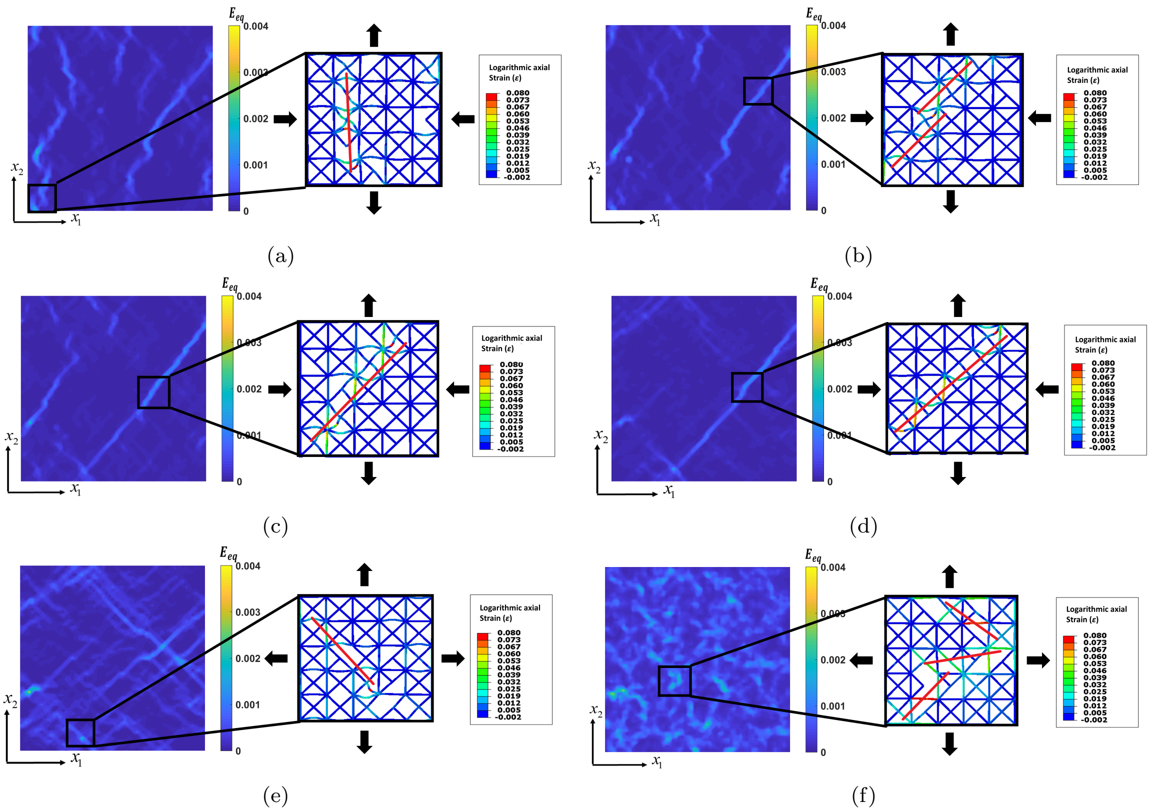

Figure 12: 5% missing lattices at the point of failure illustrating failure mechanisms on continuum and lattice level at triaxiality (a) $T = -0.2$, (b) $T = -0.1$, (c) $T = 0.0$, (d) $T = 0.2$, (e) $T = 0.4$ and (f) $T = 0.67$

4.5. Effect of triaxiality on band orientation

Figure 14 shows the variations of band orientation with triaxiality for the imperfect lattices. Figure 14 (a) is a typical example for the 5% missing struts lattice, showing band orientation under pure shear loading ($T = 0$), and Figure 14 (b) is a band orientation verses triaxiality plot for all types of defect. Band orientation can be divided into three subgroups where the imperfect lattices show a correlation between band orientation and a particular failure mechanism. The band orientation angles are greater than 60° for failure associated with crushing band or void coalescence induced failure. An orientation range 30° to 60° is associated with failure Mechanisms 2, 3 and 4. A band orientation of 0° is associated with those cases where there is no localized shear banding or cluster coalescence. The lattices with 15% distorted struts showed high variability and dependency on triaxiality of band orientation. The band orientation trend for the 30% distorted lattice is close to that of the 5% missing struts lattice and shows a linearly decreasing trend.

5. Conclusion

A novel numerical framework has been developed to investigate the various different failure mechanisms seen in perfect and imperfect planar FCC truss lattice metamaterials under different conditions of stress triaxiality, for the first time. It is seen that the

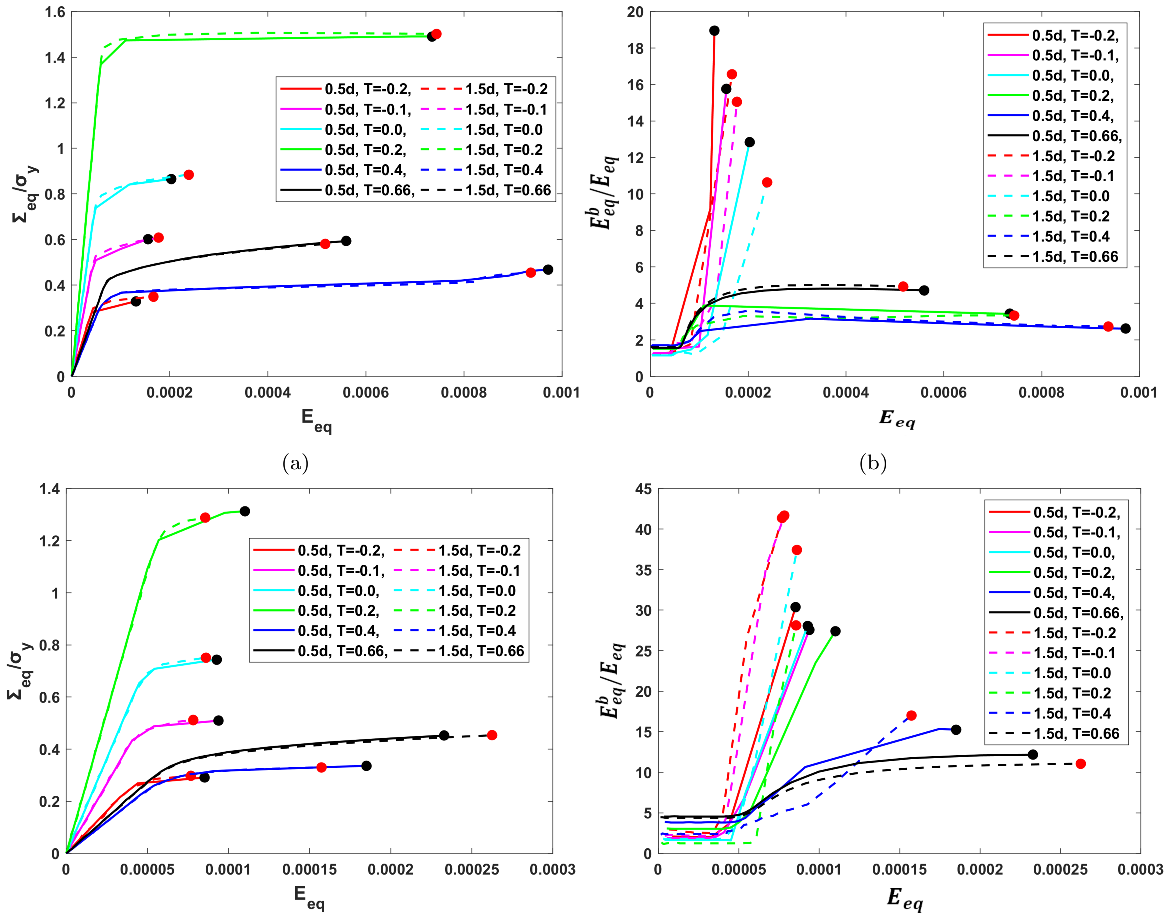

(a) (b) (c) (d)

Figure 13: Macroscopic mechanical responses of the lattice with 15% distortion (a) and the lattice with 5% missing struts (c); and evolution of equivalent band strain for the lattice with 15% distortion (b) and the lattice with 5% missing struts (d) at 0.5d and 1.5d.

mechanical response and mechanisms leading to failure are highly dependent on the state of stress triaxiality, the type and quantity of defects. In order to help understand these dependencies a classification of failure mechanisms were introduced, as shown in Figure 3. The relationships between defect type, triaxiality and failure mechanisms are summarized below.

- For triaxiality $T \leq -0.2$, crushing band dominated failure (Mechanism 1) occurs for all lattices, while for triaxiality $-0.2 < T \leq 0$, only the perfect lattice fails due to Mechanism 1. At triaxiality $-0.2 < T \leq 0$, the 15% distorted lattices show shear band localization (Mechanism 2), while at triaxiality $T > 0$ they do not show any localization. However, the 30% distorted lattice is more inclined towards shear band localization dominated failure mechanisms (Mechanism 2).

- The 5% and 10% missing strut lattices exhibit a variety of different failure mechanisms dependent on loading scenario. The 10% missing struts lattice tends to fail early owing to void coalescence (Mechanism 4) and the 5% missing struts lattice fails owing to shear band localization (Mechanism 3). For triaxiality $T > 0.2$,

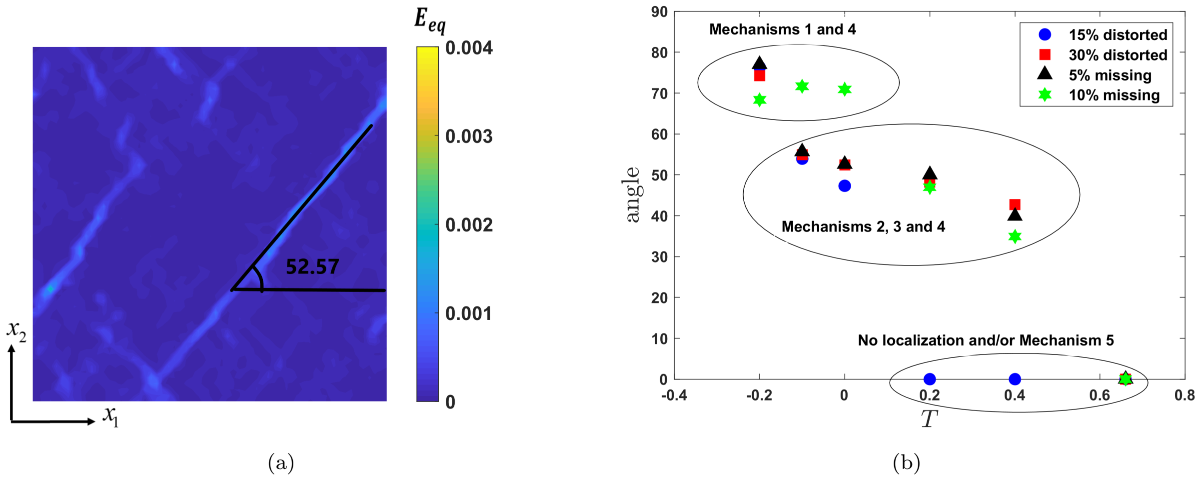

Figure 14: (a) Shear band orientation of 5% missing struts defects at T=0 and (b) triaxiality affecting shear band orientation as per type of defects.

Mechanism 5 and/or no localization are observed, independent of the number of missing struts in this range.

- The severity of onset of localization and coalescence shows dependence on lattice defect type: missing type defects are more prone to localization compared to distorted defects. It is shown that a higher percentage distribution of irregularity gives higher normalized band strain.

- The response of the lattices is not sensitive to strut diameter variations within the range of the strut diameters.

- Failure associated with void coalescence has a wider range of band orientation than seen with the other failure mechanisms, with a band orientation in the range of 30° to 60°.

Note that in this study we have assumed that the failure of RVE occurs when the maximum failure strain is reached for any strut within the RVE. Further research is needed to consider the effect of the parent material damage and any defect interaction effects when multiple types and sizes of effect are present.

Acknowledgments

The authors acknowledge the financial support from the Leverhulme Trust through Research Grant Scheme (RPG-2020-235) and the University of Nottingham for the Dean of Engineering Research Scholarship for International Excellence for Akash Bhuwal.

Appendix A.

Plastic collapse surface and effective stress-strain for rigid perfect FCC truss lattices

The theoretical framework to construct continuum constitutive model for octet-truss lattice materials were provided by [42]. The same methodology is being used to obtain elastic properties of FCC truss lattice. The FCC unit cell along with its unit vectors is sketched in Figure A.1. Let **N** define the linear transformation that relates macroscopic strains to microscopic strains under small strain deformation. The components of **N** can be determined by the components of tensor for the strut member, i.e.

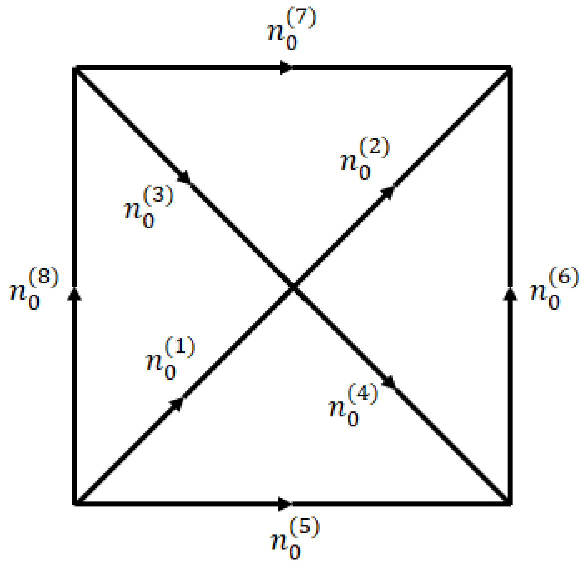

Figure A.1: FCC unit cell and its unit vectors

$$\{\mathbf{N}\}_{ij} = \begin{cases} \left\{n_0^{(i)} \otimes n_0^{(i)}\right\}_{jj}, & \text{for } j = 1, 2 \\ \left\{n_0^{(i)} \otimes n_0^{(i)}\right\}_{12}, & \text{for } j = 3 \end{cases} \tag{A.1}$$

where unit vector $n_0^{(i)}$ is aligned with the initial direction of the longitudinal axis of the strut. The macroscopic strain vector, $\mathrm{E} = [E_{11}, E_{22}, 2E_{12}]$, and microscopic strain vector, $\varepsilon = [\varepsilon^{(1)}, \varepsilon^{(2)}, \varepsilon^{(3)}, \varepsilon^{(4)}, \varepsilon^{(5)}, \varepsilon^{(6)}, \varepsilon^{(7)}, \varepsilon^{(8)}]$ can be summarized as:

$$\varepsilon = \mathbf{N}\mathrm{E} \tag{A.2}$$

The macroscopic stress vector, $\Sigma = [\Sigma_{11}, \Sigma_{22}, \Sigma_{12}]$, can be written using transpose of localized strain matrix in the form of microscopic stress vector,
$\sigma = \left[\sigma^{(1)}, \sigma^{(2)}, \sigma^{(3)}, \sigma^{(4)}, \sigma^{(5)}, \sigma^{(6)}, \sigma^{(7)}, \sigma^{(8)}\right]$:

$$\Sigma = \mathbf{c}_0\mathbf{N}^T\sigma \tag{A.3}$$

At macroscale, the elastic stress-strain relationship can be given as:

$$\Sigma = \mathbf{K}\mathrm{E}, \qquad \text{or} \qquad \mathrm{E} = \mathbf{K}^{-1}\Sigma \tag{A.4}$$

where $\mathbf{K}$ is the symmetric macroscopic stiffness tensor of the lattice material and is given as:

$$\mathbf{K} = E\mathbf{c}_0\mathbf{N}^T\mathbf{N} \tag{A.5}$$

where $\mathbf{c_0}$ is the diagonal matrix consisting volume fractions of each struts and E is elastic modulus of the parent material.

Table A.1: Components $n^{(i)_1}$ and $n^{(i)_2}$ of i^{th} unit vectors $n^{(i)}$ of individual beam members within unit cell

	$n_0^{(1)}$	$n_0^{(2)}$	$n_0^{(3)}$	$n_0^{(4)}$	$n_0^{(5)}$	$n_0^{(6)}$	$n_0^{(7)}$	$n_0^{(8)}$
$n_1^{(i)}$	$1/\sqrt{2}$	$1/\sqrt{2}$	$1/\sqrt{2}$	$1/\sqrt{2}$	1	0	1	0
$n_2^{(i)}$	$1/\sqrt{2}$	$1/\sqrt{2}$	$-1/\sqrt{2}$	$-1/\sqrt{2}$	0	1	0	1

Components of unit vector of unit cell are given in Table A.1 and from this stiffness tensor of FCC truss lattice can be given as

$$\mathbf{K} = \begin{bmatrix} K_{11} & K_{12} & K_{13} \\ K_{21} & K_{22} & K_{23} \\ K_{31} & K_{32} & K_{33} \end{bmatrix} = E \begin{bmatrix} 0.0354 & 0.0146 & 0 \\ 0.0146 & 0.0354 & 0 \\ 0 & 0 & 0.0146 \end{bmatrix} \tag{A.6}$$

From Equations (A.2) to (A.5) at microscale under elastic limit stress tensor can be rewritten as:

$$\sigma = \mathrm{N}\mathbf{K}^{-1}\Sigma \tag{A.7}$$

Figure A.2 shows the effects of imperfection on macroscopic stiffness for 20 different RVE resolutions using the method described in Section 2. K_{ij} and K^*_{ij} denote the components of the microscopic stiffness tensor defined in Equation (A.7), for the perfect and imperfect lattices, respectively. The percentage differences have been calculated against the perfect lattice. As the irregularity increases in lattice structures, there are up to 7% decrease in elastic modulus, and up to 14% increase in shear modulus for distorted defects, whereas no significant changes have been observed in elastic modulus for missing strut defects. A perfect FCC truss lattice exhibits in-plane orthotropic material behaviour, i.e. $K_{13} = K_{31} = 0, K_{23} = K_{32} = 0$. Figures A.2 (c) and (d) show the variations of K^*_{13} and K^*_{23} normalized by K_{11}, which suggests that defects can only incur small variations of K^*_{13} and K^*_{23}. As $K^*_{13} = K^*_{31}$ and $K^*_{23} = K^*_{32}$, the results confirm that the material remains in-plane orthotropic after incorporating the defects.

This microscopic stress equation has been used to establish plastic yielding of struts.

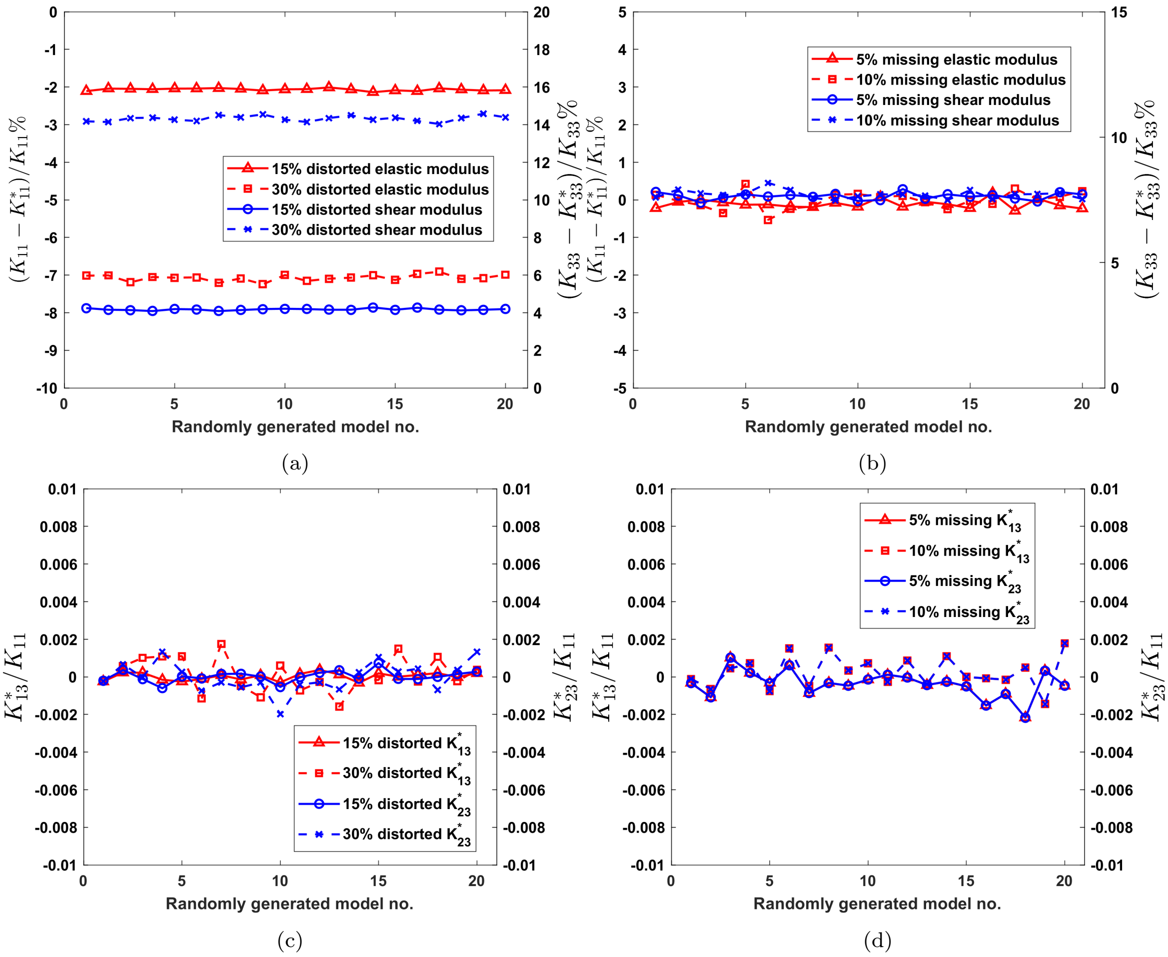

Figure A.2: Macroscopic elastic and shear modulus variation due to defects in FCC truss lattices (a) for distorted struts, (b) for missing struts, and orthotropic material properties variation due to defects in FCC truss lattices, (c) for distorted struts, and (d) for missing struts with respect to perfect lattice.

We will calculate plastic collapse surface of the FCC truss lattice under combination of multiaxial loadings and proceed to establish a Hill's model-based calculation of the equivalent plastic strain.

Plastic collapse surface

In the analytical solution we have assumed that the struts are pin-jointed and made from rigid, ideally plastic material. The accuracy of analytical solution has been validated using FE calculations. In the FE analysis each uniform cylindrical strut has been modelled by 50 Timoshenko beam elements (B21 element in ABAQUS) and has equal length in horizontal and vertical direction. The strength of stretch dominated lattice structure with 10% relative density shows three times stronger than the foam compared to bending dominated foams [37, 38]. Hence the value of relative density has been taken as 0.10 for our investigation [39]. The material was assumed to be elastic-plastic following RambergOsgood Equation (21) with hardening exponent $n = 100$ during FE calculations. The FE simulations has been terminated when local strut stress reaches yield stress $\sigma_y = 168\text{MPa}$ of parent material. The macroscopic collapse stress is calculated from Equation (A.7) equating microscopic stress to yield stress.

To calculate the yield surface under the combination of Σ_{11} and Σ_{22}, Equation (A.7) was employed with $\Sigma_{12} = 0$, i.e.

$$\begin{aligned}
\sigma^{(1)} &= \sigma^{(2)} = \sigma^{(3)} = \sigma^{(4)} = 10\Sigma_{11} + 10\Sigma_{22} = |\sigma_y| \\
\sigma^{(5)} &= \sigma^{(7)} = 34\Sigma_{11} - 14\Sigma_{22} = |\sigma_y| \\
\sigma^{(6)} &= \sigma^{(8)} = -14\Sigma_{11} + 34\Sigma_{22} = |\sigma_y|
\end{aligned} \tag{A.8}$$

Similarly, to calculate yield surface under pure shear ($\Sigma_{11} = \Sigma_{22} = 0, \Sigma_{12} \neq 0$), i.e.

$$\begin{aligned}
\sigma^{(1)} &= \sigma^{(2)} = 34\Sigma_{12} = |\sigma_y| \\
\sigma^{(3)} &= \sigma^{(4)} = -34\Sigma_{12} = |\sigma_y| \\
\sigma^{(5)} &= \sigma^{(6)} = \sigma^{(7)} = \sigma^{(8)} = 0
\end{aligned} \tag{A.9}$$

where $\sigma^{(i)}$ is local axial stress of i^{th} strut shown in Figure A.1. The macroscopic yield stresses were calculated for a variety of proportional stress paths and plotted in the relevant stress space to give the plastic collapse surface. The plastic collapse surface under combinations of applied stress $(\Sigma_{11}, \Sigma_{22})$ obtained from Equations (A.8) and (A.9) has been plotted in Figure A.3.

The FE calculations has been included in Figure A.3 shows good agreement with analytical solution. Note that plastic collapse of FCC truss lattices is driven by horizontal and vertical struts in this space, which has also been observed in FE calculations.

Anisotropic plastic strain

In this section we will use Hill's generalization of von Mises yield criterion for materials with anisotropic property. With respect to the principal axes of anisotropy, Hill's yield

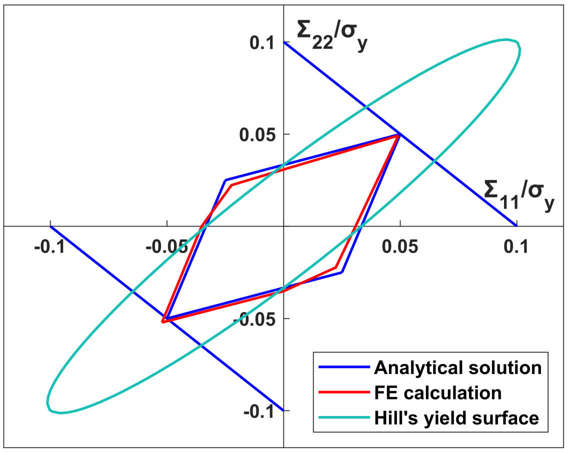

Figure A.3: Comparison between the analytical, FE and Hill's yield criterion predictions of plastic collapse surface

criteria have the form:

$$\Phi \equiv \Sigma_{eq}^2 - 1 = 0 \tag{A.10}$$

where the applied macroscopic stress is characterized by the equivalent stress measure given by for 2-dimensional space [43]:

$$\Sigma_{eq} = \sqrt{(G+H)\Sigma_{11}^2 + (F+H)\Sigma_{22}^2 - 2H\Sigma_{11}\Sigma_{22} + 2I\Sigma_{12}^2} \tag{A.11}$$

In above equation F, G, H, and I are material constants which characterize the degree of anisotropy and can be expressed as [36]:

$$\begin{aligned} F &= \frac{(\sigma_y)^2}{2}\left[\frac{1}{\left(\Sigma_{22}^y\right)^2} + \frac{1}{\left(\Sigma_{33}^y\right)^2} - \frac{1}{\left(\Sigma_{11}^y\right)^2}\right] \\ G &= \frac{(\sigma_y)^2}{2}\left[\frac{1}{\left(\Sigma_{33}^y\right)^2} + \frac{1}{\left(\Sigma_{11}^y\right)^2} - \frac{1}{\left(\Sigma_{22}^y\right)^2}\right] \\ H &= \frac{(\sigma_y)^2}{2}\left[\frac{1}{\left(\Sigma_{11}^y\right)^2} + \frac{1}{\left(\Sigma_{22}^y\right)^2} - \frac{1}{\left(\Sigma_{33}^y\right)^2}\right] \\ I &= \frac{3(\sigma_y)^2}{2\left(\Sigma_{12}^y\right)^2} \end{aligned} \tag{A.12}$$

From Equations (A.8) and (A.9) one can calculate uniaxial and shear yield strengths $(\Sigma_{11}^y, \Sigma_{22}^y, \Sigma_{12}^y)$ with respect to material principal axes. The out of plane yield strength has been taken as $\Sigma_{33}^y = 0.1\sigma_y$ (0.1 is the relative density of FCC truss lattice) to calculate material constants. Equation (A.11) has been plotted in Figure A.3 and shows a reasonably good agreement with analytical and FE solutions under combination of tension and compression. However, it dramatically overestimates the yield surface under biaxial tension and compression. The Hill's criterion has been explored in this paper to show FCC truss lattice anisotropic behaviour and to establish equivalent plastic strain equation for anisotropic material. From these parameters we can calculate equivalent plastic strain of an anisotropic material, using work conjugation given as [36]:

$$E_{eq} = \sqrt{\frac{1}{FH + FG + GH} \left[(F + H) (E_{11})^2 + 2H (E_{11} E_{22}) + (G + H) (E_{22})^2 \right] + \frac{2 (E_{12})^2}{I}} \tag{A.13}$$

The above equation has been extensively used to quantify localization and coalescence in this paper.

Appendix B.

Results comparison - ABAQUS Standard vs. Explicit solver

For constant triaxiality, stress ratio equation for ABAQUS Standard solver can be written from Equation (11) as:

$$\begin{aligned} &\rho = \frac{\Sigma_{11}}{\Sigma_{22}} = \text{ const } \Rightarrow \frac{\left(u_1^{N_1} - u_1^M\right)\left(\overline{W}_1 + u_1^M\right) d}{\left(u_2^{N_2} - u_2^M\right)\left(\overline{W}_2 + u_2^M\right) d} = \rho \\ &\text{OR} \\ &u_1^{N_1} = u_1^M + \rho \frac{\left(\overline{W}_2 + u_2^M\right)}{\left(\overline{W}_1 + u_1^M\right)} \left(u_2^{N_2} - u_2^M\right) \end{aligned} \tag{B.1}$$

Note that above equation is independent of spring constants and $u_2^{N_2}$ is a prescribed value. For the simulation, we have taken spring constant k_i equals to $10^{-7} \times E \times W_1$ (E is parent material's Young's modulus). ABAQUS Standard calculates three unknows quantities u_1^M, u_2^M and u_2^M using MPC (multi-point constraints) user sub-routine, iteratively. Figure B.1 shows that results obtained through explicit solver are comparable with standard solver for triaxiality $T = 0.4$ and 0.66.

Appendix C.

Continuum level FEA modelling of beam elements

The nodal displacement vectors were extracted from ABAQUS and these displacement vectors have been used as input for 2D triangular solid elements. Then strains have been mapped using the second order Gauss-Quadrature method which can be expressed as:

$$\mathbf{E}^e = \mathbf{B}^e \mathbf{a}^e \tag{C.1}$$

where $\mathbf{a}^e$ is nodal vector of the element subjected to displacement components u_1 and u_2,

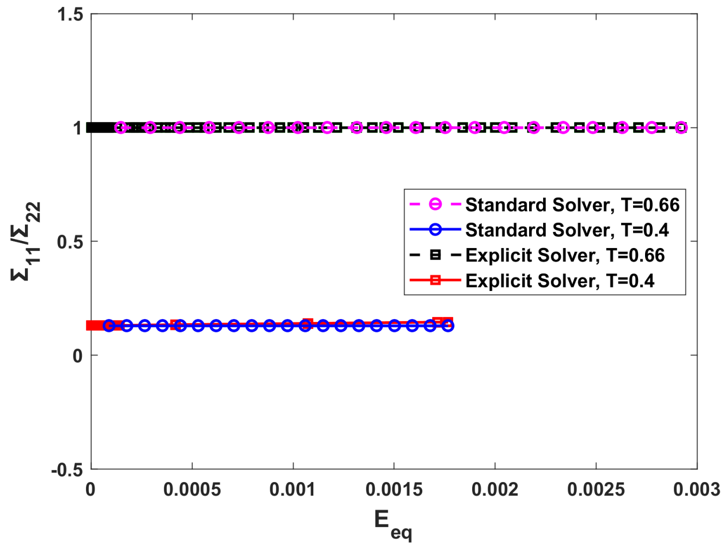

Figure B.1: Stress ratio comparison obtained via ABAQUS Standard and Explicit solvers

and $\mathbf{B}^e$ is derivatives of shape function given by:

$$\mathbf{B}^e = \begin{bmatrix} \frac{\partial N_1^e}{\partial x_1} & 0 & \frac{\partial N_2^e}{\partial x_1} & 0 & \cdots & \frac{\partial N_{en}^e}{\partial x_1} & 0 \\ 0 & \frac{\partial N_1^e}{\partial x_2} & 0 & \frac{\partial N_2^e}{\partial x_2} & \cdots & 0 & \frac{\partial N_{en}^e}{\partial x_2} \\ \frac{\partial N_1^e}{\partial x_2} & \frac{\partial N_1^e}{\partial x_1} & \frac{\partial N_2^e}{\partial x_2} & \frac{\partial N_2^e}{\partial x_1} & \cdots & \frac{\partial N_{en}^e}{\partial x_2} & \frac{\partial N_{en}^e}{\partial x_1} \end{bmatrix} \tag{C.2}$$

where n_{en} is the number of nodes of one element and N^e is the elemental shape function of the respective nodes. The strain components at Gauss points inside the band is used to calculate the average equivalent strain using Equation (A.13). To evaluate out of plane strain field, we have used standard mechanics approach within RVE. The relationship between the average strain of a triangular element and beam elements connected to the vertices of the triangular element can be expressed as:

$$E_{33}^e = \sum_{i=1}^{3} c_i \varepsilon_{33}^i \tag{C.3}$$

Similarly, for RVE the out of plane strain can be written as:

$$E_{33}^{RVE} = \sum_{j=1}^{N} c_j E_{33}^e \tag{C.4}$$

where c_i and c_j are volume fractions of the i^{th} beam element and the j^{th} triangular element respectively; N the total number of the triangular elements and ε_{33}^i the out of plane strain for the i^{th} beam element which can be calculated using volume conservation.

Appendix D.

Effect of imperfection on onset of localization and lattice failure

Figures D.1 (a) and (b) show the normalized equivalent band strain E^b_{eq}/E_{eq} as a function of triaxiality T, at the instants of onset of localization and final failure, respectively, under the triaxiality range $-0.2 \leq T \leq 0.67 \quad (\Sigma_{22} > 0)$, for perfect and imperfect lattices. There are three zones that can distinguish the failure mechanisms: Zone I ($T \leq -0.2$) represents compressive loading dominated behaviour, Zone II ($-0.2 < T < 0.2$) the shear loading dominated behaviour, and Zone III the tensile loading dominated behaviour.

In Zone I ($T \leq -0.2$), crushing band dominated failure mode occurs for all lattices. The normalized equivalent band strains are lowest compared to other failure mechanisms at onset of localization (Figure D.1 (a)); however, all types of lattice structures fail at much higher normalized equivalent band strain because of crushing band compared to other types of failure mechanisms (Figure D.1 (b)).

The perfect lattice – The normalized equivalent band strain for perfect lattices is around ~ 1 at onset of localization (Figure D.1 (a)); and at all triaxialities, the perfect lattice shows independency for onset of localization. In Figure D.1 (b), the perfect lattice shows continuous decrease in band strain. The crushing band formulation shows higher band strain at time of failure and after triaxiality $T \geq 0$, localization does not occur resulting in a flattened curve.

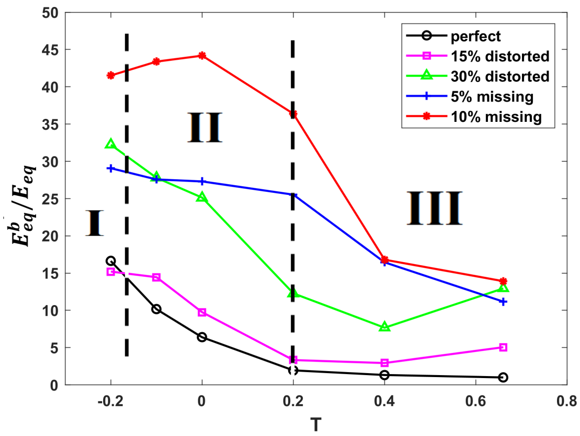

(a)

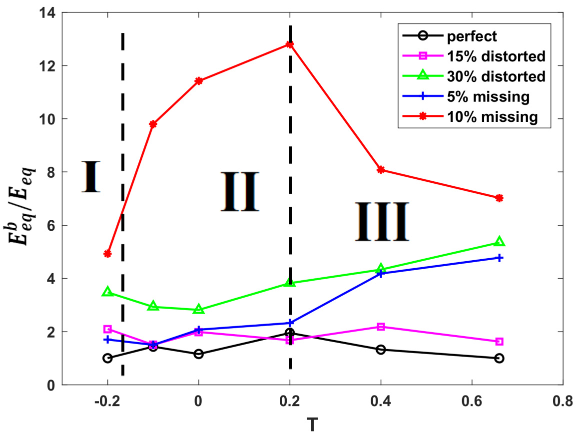

(b)

Figure D.1: Value of normalized equivalent band strain at onset of localization and (b) at the point of failure as a function of triaxiality

Distorted lattices– For the 15% distorted lattice, the normalized equivalent band strains are not changing substantially through all triaxialities (Figure D.1 (a)). This indicates that the onset of localization is nearly independent of triaxiality for the 15% distorted lattices. The 30% distorted lattice shows Mechanism 2 dominated failure for triaxiality $0 \leq T \leq 0.4$, and they are more inclined to shear band formulation compared to 15% distorted lattices. At triaxiality $T = 0.67$, multiple high equivalent strain areas form, as the same as the 15% distorted lattice but at a higher equivalent band strain due to higher degree of irregularity. Hence, from Zone II to Zone III the normalized band strain is increasing continuously (Figure D.1 (a)). Figure D.1 (b) shows the decreasing trend in normalized equivalent band strain at the time of failure, which indicates that crushing band shows maximum band strain followed by shear band localization at the time of failure. Like perfect lattices, for triaxiality $T > 0$, localization does not occur, resulting in a flattened curve for the 15% distorted lattice. The trend of 30% distorted lattice is the same as the 15% distorted lattice albeit at higher maximum normalized equivalent band strain, which implies dependency of degree of irregularity on the final failure.

Missing lattices – From Figure D.1 (a), the 5% missing lattice shows that, in Zone I and Zone II, the normalized equivalent band strains are not changing substantially at onset of localization, indicating that the onset of localization is independent of triaxiality. In Zone III the normalized equivalent band strain increases due to void coalescence dominated failure (Mechanisms 5). For the 10% missing lattice, from Zone I to Zone II, the band strains at onset of localization increase owing to the change from failure Mechanism 1 to Mechanism 4. The slight decrease in normalized equivalent band strain at triaxiality $T = 0.67$ (biaxial tension) represent the absence of shear band and failure dictated by cluster coalescence only (Mechanism 5). For all triaxialities, for the 10% missing lattices, the strain localization occurs at higher normalized equivalent band strain compared to the 5% missing lattices. Thus, the number of missing struts is crucial for the strain localization. In Figure D.1 (b), the 10% missing lattice shows that the maximum normalized equivalent band strain is higher than 5% missing lattice at the time of final failure. It shows that the 10% missing lattices are more prone to crushing band (Mechanism 1) and shear band (Mechanism 4) formulation compared to 5% missing lattices before final failure occurs. In Zone III, the changes in number of missing struts show no significant difference, which signifies that failure Mechanism 4 and Mechanism 5 are nearly independent of number of missing struts in this range.

References

[1] M. K. Thompson, G. Moroni, T. Vaneker, G. Fadel, R. I. Campbell, I. Gibson, A. Bernard, J. Schulz, P. Graf, B. Ahuja, F. Martina, Design for Additive Manufacturing: Trends, opportunities, considerations, and constraints, CIRP Annals - Manufacturing Technology (2016). doi:10.1016/j.cirp.2016.05.004.

[2] D. W. Rosen, Computer-Aided Design for Additive Manufacturing of Cellular Structures, Computer-Aided Design and Applications (2007). doi:10.1080/16864360.2007.10738493.

[3] A. Panesar, M. Abdi, D. Hickman, I. Ashcroft, Strategies for functionally graded lattice structures derived using topology optimisation for Additive Manufacturing, Additive Manufacturing (2018). doi:10.1016/j.addma.2017.11.008.

[4] I. Maskery, I. A. Ashcroft, The deformation and elastic anisotropy of a new gyroid-based honeycomb made by laser sintering, Additive Manufacturing (2020). doi:10.1016/j.addma.2020.101548.

[5] I. Maskery, A. O. Aremu, L. Parry, R. D. Wildman, C. J. Tuck, I. A. Ashcroft, Effective design and simulation of surface-based lattice structures featuring volume fraction and cell type grading, Materials and Design (2018). doi:10.1016/j.matdes.2018.05.058.

[6] P. Köhnen, C. Haase, J. Bültmann, S. Ziegler, J. H. Schleifenbaum, W. Bleck, Mechanical properties and deformation behavior of additively manufactured lattice structures of stainless steel, Materials and Design (2018). doi:10.1016/j.matdes.2018.02.062.

[7] A. Vigliotti, V. S. Deshpande, D. Pasini, Non linear constitutive models for lattice materials, Journal of the Mechanics and Physics of Solids (2014). doi:10.1016/j.jmps.2013.10.015.

[8] X. Geng, Y. Lu, C. Liu, W. Li, Z. Yue, Fracture characteristic analysis of cellular lattice structures under tensile load, International Journal of Solids and Structures (2019). doi:10.1016/j.ijsolstr.2019.01.006.

[9] H. Alsalla, L. Hao, C. Smith, Fracture toughness and tensile strength of 316L stainless steel cellular lattice structures manufactured using the selective laser melting technique, Materials Science and Engineering A (2016). doi:10.1016/j.msea.2016.05.075.

[10] B. Vayre, F. Vignat, F. Villeneuve, Metallic additive manufacturing: State-of-the-art review and prospects, Mechanics and Industry (2012). doi:10.1051/meca/2012003.

[11] Z. S. Bagheri, D. Melancon, L. Liu, R. B. Johnston, D. Pasini, Compensation strategy to reduce geometry and mechanics mismatches in porous biomaterials built with Selective Laser Melting, Journal of the Mechanical Behavior of Biomedical Materials (2017). doi:10.1016/j.jmbbm.2016.04.041.

[12] S. Arabnejad, D. Pasini, Mechanical properties of lattice materials via asymptotic homogenization and comparison with alternative homogenization methods, International Journal of Mechanical Sciences (2013). doi:10.1016/j.ijmecsci.2013.10.003.

[13] A. Vigliotti, D. Pasini, Stiffness and strength of tridimensional periodic lattices, Computer Methods in Applied Mechanics and Engineering (2012). doi:10.1016/j.cma.2012.03.018.

[14] L. Liu, P. Kamm, F. García-Moreno, J. Banhart, D. Pasini, Elastic and failure response of imperfect three-dimensional metallic lattices: the role of geometric defects induced by Selective Laser Melting, Journal of the Mechanics and Physics of Solids (2017). doi:10.1016/j.jmps.2017.07.003.

[15] S. Wehmeyer, F. W. Zok, C. Eberl, P. Gumbsch, N. Cohen, R. M. McMeeking, M. R. Begley, Post-buckling and dynamic response of angled struts in elastic lattices, Journal of the Mechanics and Physics of Solids 133 (2019) 103693. doi:https://doi.org/10.1016/j.jmps.2019.103693.
URL https://www.sciencedirect.com/science/article/pii/S0022509619303758

[16] T. Tancogne-Dejean, A. B. Spierings, D. Mohr, Additively-manufactured metallic micro-lattice materials for high specific energy absorption under static and dynamic loading, Acta Materialia (2016). doi:10.1016/j.actamat.2016.05.054.

[17] G. Campoli, M. S. Borleffs, S. Amin Yavari, R. Wauthle, H. Weinans, A. A. Zadpoor, Mechanical properties of open-cell metallic biomaterials manufactured using additive manufacturing, Materials and Design (2013). doi:10.1016/j.matdes.2013.01.071.

[18] I. Barsoum, J. Faleskog, Micromechanical analysis on the influence of the Lode parameter on void growth and coalescence, International Journal of Solids and Structures (2011). doi:10.1016/j.ijsolstr.2010.11.028.

[19] M. Dunand, D. Mohr, Effect of Lode parameter on plastic flow localization after proportional loading at low stress triaxialities, Journal of the Mechanics and Physics of Solids (2014). doi:10.1016/j.jmps.2014.01.008.

[20] F. Scheyvaerts, P. R. Onck, C. Tekoğlu, T. Pardoen, The growth and coalescence of ellipsoidal voids in plane strain under combined shear and tension, Journal of the Mechanics and Physics of Solids (2011). doi:10.1016/j.jmps.2010.10.003.

[21] V. Tvergaard, Ductile fracture by cavity nucleation between larger voids, Journal of the Mechanics and Physics of Solids (1982). doi:10.1016/0022-5096(82)90033-3.

[22] V. Tvergaard, Shear deformation of voids with contact modelled by internal pressure, International Journal of Mechanical Sciences (2008). doi:10.1016/j.ijmecsci.2008.08.007.

[23] P. M. Anderson, N. A. Fleck, K. L. Johnson, Localization of plastic deformation in shear due to microcracks, Journal of the Mechanics and Physics of Solids (1990). doi:10.1016/0022-5096(90)90028-3.

[24] C. Tekolu, J. W. Hutchinson, T. Pardoen, On localization and void coalescence as a precursor to ductile fracture, Philosophical Transactions of the Royal Society A: Mathematical, Physical and Engineering Sciences (2015). doi:10.1098/rsta.2014.0121.

[25] I. Echeta, X. Feng, B. Dutton, R. Leach, S. Piano, Review of defects in lattice structures manufactured by powder bed fusion, International Journal of Advanced Manufacturing Technology (2020). doi:10.1007/s00170-019-04753-4.

[26] B. Zhang, Y. Li, Q. Bai, Defect Formation Mechanisms in Selective Laser Melting: A Review (2017). doi:10.1007/s10033-017-0121-5.

[27] D. Melancon, Z. S. Bagheri, R. B. Johnston, L. Liu, M. Tanzer, D. Pasini, Mechanical characterization of structurally porous biomaterials built via additive manufacturing: experiments, predictive models, and design maps for load-bearing bone replacement implants, Acta Biomaterialia (2017). doi:10.1016/j.actbio.2017.09.013.

[28] N. E. Romijn, N. A. Fleck, The fracture toughness of planar lattices: Imperfection sensitivity, Journal of the Mechanics and Physics of Solids (2007). doi:10.1016/j.jmps.2007.04.010.

[29] B. Su, Z. Zhou, Z. Wang, Z. Li, X. Shu, Effect of defects on creep behavior of cellular materials, Materials Letters (2014). doi:10.1016/j.matlet.2014.07.185.

[30] C. Chen, T. J. Lu, N. A. Fleck, Effect of inclusions and holes on the stiffness and strength of honeycombs, International Journal of Mechanical Sciences (2001). doi:10.1016/S0020-7403(99)00122-8.

[31] B. Lozanovski, M. Leary, P. Tran, D. Shidid, M. Qian, P. Choong, M. Brandt, Computational modelling of strut defects in SLM manufactured lattice structures, Materials and Design (2019). doi:10.1016/j.matdes.2019.107671.

[32] S. Arabnejad, R. Burnett Johnston, J. A. Pura, B. Singh, M. Tanzer, D. Pasini, High-strength porous biomaterials for bone replacement: A strategy to assess the interplay between cell morphology, mechanical properties, bone ingrowth and manufacturing constraints, Acta Biomaterialia (2016). doi:10.1016/j.actbio.2015.10.048.

[33] R. C. Lin, D. Steglich, W. Brocks, J. Betten, Performing RVE calculations under constant stress triaxiality for monotonous and cyclic loading, International Journal for Numerical Methods in Engineering (2006). doi:10.1002/nme.1600.

[34] ABAQUS, Abaqus 6.14, Abaqus 6.14 Analysis User's Guide (2014).

[35] W. Wu, J. Owino, A. Al-Ostaz, L. Cai, Applying Periodic Boundary Conditions in Finite Element Analysis, Simulia Community Conference (2014).

[36] R. Hill, A theory of the yielding and plastic flow of anisotropic metals, Proceedings of the Royal Society of London. Series A. Mathematical and Physical Sciences 193 (1033) (1948) 281–297. doi:10.1098/rspa.1948.0045.

[37] V. S. Deshpande, M. F. Ashby, N. A. Fleck, Foam topology: Bending versus stretching dominated architectures, Acta Materialia (2001). doi:10.1016/S1359-6454(00)00379-7.

[38] I. Gibson, D. W. Rosen, B. Stucker, Additive manufacturing technologies: Rapid prototyping to direct digital manufacturing, 2010. doi:10.1007/978-1-4419-1120-9.

[39] H. C. Tankasala, V. S. Deshpande, N. A. Fleck, Tensile response of elastoplastic lattices at finite strain, Journal of the Mechanics and Physics of Solids (2017). doi:10.1016/j.jmps.2017.02.002.

[40] I. Rosenthal, A. Stern, N. Frage, Microstructure and Mechanical Properties of AlSi10Mg Parts Produced by the Laser Beam Additive Manufacturing (AM) Technology, Metallography, Microstructure, and Analysis (2014). doi:10.1007/s13632-014-0168-y.

[41] N. Cohen, K. Bhattacharya, A numerical study of the electromechanical response of liquid metal embedded elastomers, International Journal of Non-Linear Mechanics 108 (October 2018) (2019) 81–86. doi:10.1016/j.ijnonlinmec.2018.10.011.
URL https://doi.org/10.1016/j.ijnonlinmec.2018.10.011

[42] D. Mohr, Mechanism-based multi-surface plasticity model for ideal truss lattice materials, International Journal of Solids and Structures (2005). doi:10.1016/j.ijsolstr.2004.10.032.

[43] L. C. Reis, P. A. Prates, M. C. Oliveira, A. D. Santos, J. V. Fernandes, Anisotropy and plastic flow in the circular bulge test, International Journal of Mechanical Sciences (2017). doi:10.1016/j.ijmecsci.2017.04.007.